

Stellar Chromospheric Activity Database of Solar-like Stars Based on the LAMOST Low-Resolution Spectroscopic Survey: II. the bolometric and photospheric calibration

Weitao Zhang¹, Jun Zhang¹, Han He^{2,3}, Ali Luo^{2,3,4}, and Haotong Zhang^{2,3,4}

¹ School of Physics and Optoelectronics Engineering, Anhui University, Hefei 230601, China; e-mail: zjun@ahu.edu.cn

² National Astronomical Observatories, Chinese Academy of Sciences, Beijing 100101, China; e-mail: hehan@nao.cas.cn

³ University of Chinese Academy of Sciences, Beijing 100049, China

⁴ CAS Key Laboratory of Optical Astronomy, Chinese Academy of Sciences, Beijing 100101, China

May 24, 2024

ABSTRACT

Context. The dependence of stellar magnetic activity on stellar parameters would be inspired by the chromospheric activity studies based on the large-scale spectroscopic surveys.

Aims. The main objective of this project is to provide the chromospheric activity parameters database for the LAMOST Low-Resolution Spectroscopic Survey (LRS) spectra of solar-like stars and explore the overall property of stellar chromospheric activity.

Methods. The Ca II H and K lines are employed to construct indicators for assessing and studying the chromospheric activity of solar-like stars. We investigate the widely used bolometric and photospheric calibrated chromospheric activity index R'_{HK} , derived from the method in the classic literature ($R'_{\text{HK,classic}}$) and the method based on the PHOENIX model ($R'_{\text{HK,PHOENIX}}$). Since the detailed stellar atmospheric parameters, effective temperature (T_{eff}), surface gravity ($\log g$), and metallicity ($[\text{Fe}/\text{H}]$), are available for LAMOST, we estimate the chromospheric activity index $R'_{\text{HK,PHOENIX}}$, along with the corresponding bolometric calibrated index $R_{\text{HK,PHOENIX}}$, taking these parameters into account.

Results. We provide the database of the derived chromospheric activity parameters for 1,122,495 LAMOST LRS spectra of solar-like stars. Our calculations show that $\log R'_{\text{HK,PHOENIX}}$ is approximately linearly correlated with $\log R'_{\text{HK,classic}}$. The results based on our extensive archive support the view that the dynamo mechanism of solar-like stars is generally consistent with the Sun; and the value of solar chromospheric activity index is located at the midpoint of the solar-like star sample. We further investigate the proportions of solar-like stars with different chromospheric activity levels (very active, active, inactive and very inactive). The investigation indicates that the occurrence rate of high levels of chromospheric activity is lower among the stars with effective temperatures between 5600 and 5900 K.

Key words. stars: activity – stars: chromospheres

1. Introduction

Stellar chromospheric activity, known as the performance of stellar magnetic activity, is expected to reveal the physical mechanism of stars (Hall 2008). The emission in the line cores of Ca II H and K lines is commonly recognized to be sensitive to stellar chromospheric activity. An empirical chromospheric activity index S_{MWO} was introduced to quantify the emission of Ca II H and K lines observed in the Mount Wilson Observatory (MWO) (Wilson 1968; Vaughan et al. 1978). Since S_{MWO} is defined as the ratio between the emission flux in the line cores of Ca II H and K lines and the pseudo-continuum flux (the flux of two 20 Å reference bands in the violet and red sides), it is concise and effective for characterizing the stellar activity cycle (Wilson 1978). However, S_{MWO} is related to the continuum flux which is governed by the stellar effective temperature (or equivalently, the color index) (Middelkoop 1982). As a result, it would be inflexible for comparing the emission of Ca II H and K lines among stars of different spectral types.

The ratio between the stellar surface flux in the line core of Ca II H and K lines and the stellar bolometric flux, denoted as R_{HK} , is considered to be marginally affected by the stellar effective temperature (or the color index) and can be derived from

S_{MWO} (Linsky et al. 1979; Middelkoop 1982; Rutten 1984). Middelkoop (1982) and Rutten (1984) introduced the bolometric factor C_{cf} (depends on the color index $B - V$) and the factor K to convert S_{MWO} to the stellar surface flux in the line cores of Ca II H and K lines. Meanwhile, the photospheric fluxes contained in the line cores of Ca II H and K lines could not be ignored, especially for solar-like stars (Hartmann et al. 1984; Noyes et al. 1984). The photospheric contribution R_{phot} , which represents the photospheric flux normalized by the stellar bolometric flux, can analogously be deduced as a function of $B - V$ (Noyes et al. 1984). Subtracting R_{phot} from R_{HK} , one can derive the widely used bolometric and photospheric calibrated chromospheric activity index R'_{HK} .

The R'_{HK} is frequently employed to characterise the relationships between stellar chromospheric activity and other stellar properties such as rotation period (Noyes et al. 1984; Suárez Mascareño et al. 2015; Astudillo-Defru et al. 2017; Brown et al. 2022; Boudreaux et al. 2022) and stellar age (Mamajek & Hillenbrand 2008; Pace 2013; Lorenzo-Oliveira et al. 2018; Booth et al. 2020). The derivation of R'_{HK} may be influenced by the bolometric factor C_{cf} , the value of K , the photospheric contribution R_{phot} and S_{MWO} . Cincunegui et al. (2007) compared the rela-

tionship between the $H\alpha$ line and the Ca II H and K lines, where they recalibrated the C_{cf} to the range of $0.45 \leq B - V \leq 1.81$. Suárez Mascareño et al. (2015) and Astudillo-Defru et al. (2017) concentrated on the relationship of R'_{HK} and the rotation period for M dwarfs. Suárez Mascareño et al. (2015) extended the bolometric factor C_{cf} and the photospheric contribution R_{phot} to $B - V = 1.90$ using the empirical spectral library. Astudillo-Defru et al. (2017) derived the equations of C_{cf} and R_{phot} based on the empirical and synthetic spectral library, respectively. Lorenzo-Oliveira et al. (2018) and Marvin et al. (2023) have provided estimates of C_{cf} and R_{phot} as functions of effective temperature.

The stellar surface flux now is relatively accurately determined in synthetic spectral model such as ATLAS, PHOENIX and MARCS (Munari et al. 2005; Allard & Hauschildt 1995; Gustafsson et al. 2008). The synthetic spectral library PHOENIX was widely used in the calculation of chromospheric activity index based on the Ca II H and K lines, e.g., Mittag et al. (2013) estimated the stellar surface flux as a formula of $B - V$, and Marvin et al. (2023) derived the relationship between C_{cf} and the stellar effective temperature. Pérez Martínez et al. (2014) directly cross-matched each observed spectrum with the synthetic spectral library PHOENIX to derive an empirical chromospheric basal flux line. In addition, the PHOENIX spectral library is also used to deduce the photospheric contribution (e.g., Mittag et al. 2013; Astudillo-Defru et al. 2017; Marvin et al. 2023). Astudillo-Defru et al. (2017) pointed out that the photospheric contribution derived from the PHOENIX library is higher than that obtained from empirical spectra by Noyes et al. (1984).

With the development of large-scale photometric and spectroscopic surveys, statistical investigation of stellar chromosphere may disclose some novel phenomena (de Grijs & Kamath 2021). The Large Sky Area Multi-Object Fiber Spectroscopic Telescope (LAMOST, also named the Guoshoujing Telescope) has released massive spectral data since its pilot survey started in 2011 (Cui et al. 2012; Zhao et al. 2012; Luo et al. 2012). The spectra released by the Low-Resolution Spectroscopic Survey (LRS) of LAMOST cover the wavelength from 3700 to 9100 Å with a spectral resolving power ($R = \lambda/\Delta\lambda$) of about 1800 (Zhao et al. 2012). A number of investigations of chromospheric activity have profited from the several spectral lines recorded by LAMOST, such as the Ca II H and K lines, the $H\alpha$ line and the Ca II infrared triplet (IRT) lines (e.g., Zhang et al. 2019, 2020; Bai et al. 2021; Han et al. 2023; He et al. 2023; Huang et al. 2024). In our previous work (Zhang et al. 2022, hereafter Paper I), we investigated the Ca II H and K lines of LAMOST LRS spectra and provided a stellar chromospheric activity database, especially calibrated the S index value of LAMOST to the scale of MWO. In this work, we dedicate to describe the chromospheric activity of solar-like stars based on the bolometric and photospheric calibrated indexes of LAMOST LRS spectra (He et al. 2021).

This paper is organized as follows. In Section 2, we describe the spectral data used in this work. In Section 3, the detailed procedures of deriving the chromospheric activity indexes and their uncertainties are illustrated. In Section 4, we present the database provided in this work and discuss the chromospheric activity based on the database. Finally we provide a brief summary and conclusion of this work in Section 5.

2. Data Collection of Solar-like Stars

We use the LAMOST LRS spectra in the Data Release 8 (DR8) v2.0¹, which were observed between October 2011 and May 2020. The LAMOST DR8 v2.0 comprises 10,633,515 LRS spectra, among which 6,684,413 spectra with determined stellar parameters have been published in the LAMOST LRS Stellar Parameter Catalog of A, F, G and K Stars (hereafter referred to as the LAMOST LRS AFGK Catalog). The stellar parameters such as effective temperature (T_{eff}), surface gravity ($\log g$), metallicity ($[\text{Fe}/\text{H}]$), heliocentric radial velocity (V_r) and their corresponding uncertainties are afforded by the LAMOST Stellar Parameter Pipeline (LASP) (Luo et al. 2015).

We select the spectra of solar-like stars (Cayrel de Strobel 1996) by the effective temperatures around the Sun ($T_{\text{eff},\odot} = 5777$ K, adopted as in Ramírez et al. 2012) that are in the range of $4800 \leq T_{\text{eff}} \leq 6300$ K, and the metallicities around the Sun ($[\text{Fe}/\text{H}]_{\odot} = 0.0$ dex) that are in the range of $-1.0 < [\text{Fe}/\text{H}] < 1.0$ dex. The spectra of main-sequence stars are empirically separated from the giant sample by the criterion of $\log g$ as adopted in Paper I:

$$\log g \geq 5.98 - 0.00035 \times T_{\text{eff}}. \quad (1)$$

The uncertainties of the chromospheric activity indexes are related to the uncertainties of the spectral fluxes and the corresponding stellar parameters derived from the LRS spectra which are predominantly impacted by the signal-to-noise ratio (S/N) parameters of LRS spectra. The precision of spectral fluxes of Ca II H and K lines and stellar parameters is primarily affected by the S/N in the g and r bands of LRS. Therefore, the high-S/N spectra of solar-like stars are screened out by the S/N threshold $S/N_g \geq 50.00$ and $S/N_r \geq 71.43$ as adopted in Paper I. A total of 1,149,216 spectra of solar-like stars are picked out from the LAMOST LRS AFGK Catalog. The band of Ca II H and K lines used to derive the chromospheric activity index refer to the vacuum wavelength range of 3892.17–4012.20 Å (see Paper I). The spectra in this band with zero or negative flux are discarded. We eventually analyse the chromospheric activity based on 1,122,495 LAMOST LRS spectra of solar-like stars. The distribution of the selected spectral samples is shown in Figure 1, where the gray dots represent the samples in LAMOST LRS AFGK Catalog. Since abundant stellar information is available in Gaia DR3 (Gaia Collaboration et al. 2023), we identified 861,505 solar-like stars in the selected spectra with `gaia_source_id` obtainable in LAMOST LRS AFGK Catalog. Given the LAMOST is dedicated to the spectral survey of large sky areas, 81% of the solar-like stars have been observed only once. Figure 2 displays the histogram of the observation numbers for 861,505 solar-like stars.

In Figure 3, we show the histograms of the T_{eff} , $\log g$, $[\text{Fe}/\text{H}]$ and V_r for the 861,505 solar-like stars used in this work. If one star is observed more than once, the values of T_{eff} , $\log g$, $[\text{Fe}/\text{H}]$ and V_r are taken as the median of the corresponding values of the multiple observed spectra. As illustrated in the LAMOST DR8 release note², the uncertainties of T_{eff} , $\log g$, $[\text{Fe}/\text{H}]$ and V_r are relatively higher for S/N_r less than 30 and are relatively accurate for S/N_r greater than 50. Based on our aforementioned S/N threshold of spectral selection ($S/N_g \geq 50.00$ and $S/N_r \geq 71.43$), the uncertainties of T_{eff} , $\log g$, $[\text{Fe}/\text{H}]$ and V_r for the selected stars, which are provided by LASP, are approximately distributed around 25 K, 0.035 dex, 0.025 dex, and 3.5

¹ <http://www.lamost.org/dr8/v2.0/>

² <https://www.lamost.org/dr8/v2.0/doc/release-note>

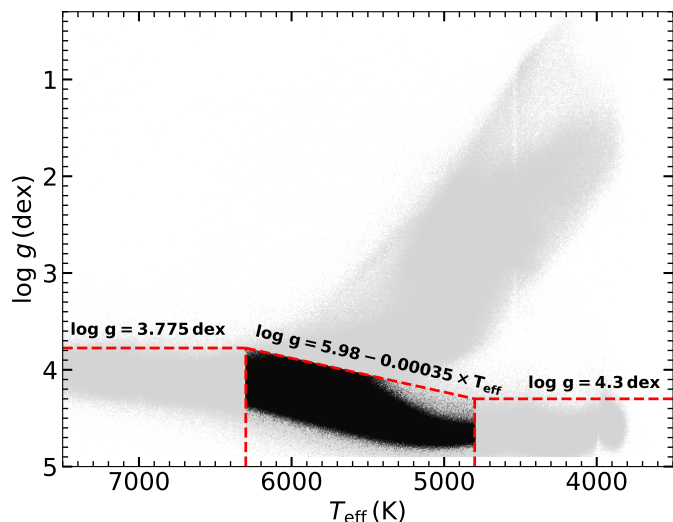


Fig. 1. The distribution of the selected spectral samples (black dots) of solar-like stars and the samples in LAMOST LRS AFGK Catalog (gray dots) with T_{eff} in the range of 3500 to 7500 K. The vertical and horizontal red lines represent the empirical selection ranges of T_{eff} and $\log g$, respectively; the diagonal red line denotes the corresponding empirical formula in Equation 1.

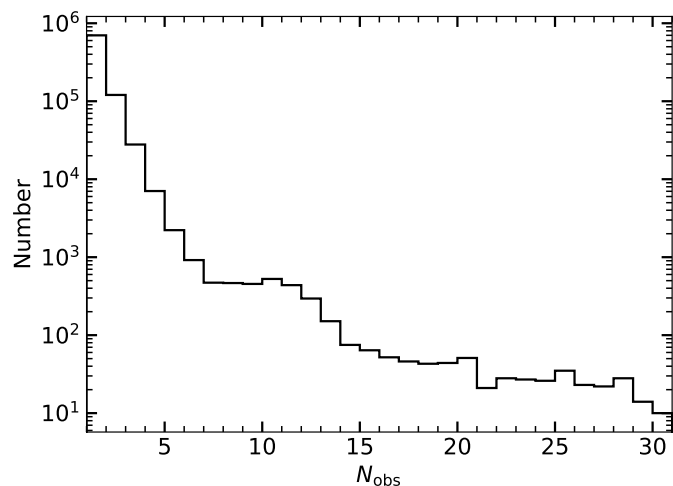


Fig. 2. Histogram of the number of observations for the 861,505 solar-like stars.

km s^{-1} , respectively. The LAMOST DR8 release note also provides the parameter comparisons between LAMOST DR8 v2.0 LRS and DR16 (Ahumada et al. 2020) of the Sloan Digital Sky Survey (York et al. 2000). Since the effective temperature plays an important role in Section 3, we compare the T_{eff} provided by LASP with the results of Amard et al. (2020) in Appendix A.

3. Evaluation of the Chromospheric Activity Index of Solar-like Star

The following steps are taken in the derivation of the chromospheric activity index R'_{HK} of solar-like stars based on the Ca II H and K lines of LAMOST LRS: (1) definition of S_{MWO} for LAMOST LRS, (2) conversion of S_{MWO} to R_{HK} , (3) derivation of the bolometric and photospheric calibrated chromospheric activity index R'_{HK} , (4) estimation of the uncertainty of chromospheric activity indexes.

3.1. Definition of S_{MWO} for LAMOST LRS

The stellar chromospheric activity index has been widely studied and broadened based on the emission of the Ca II H and K lines (e.g., Wilson 1968; Vaughan et al. 1978; Duncan et al. 1991; Baliunas et al. 1995; Hall et al. 2007; Egeland et al. 2017; Boro Saikia et al. 2018). In 1966, the two-channel HKP-1 spectrophotometer was employed in Mount Wilson Observation to monitor the emission of stellar Ca II H and K lines (Wilson 1968; Hall et al. 2007). One channel was used to collect data in the 25 Å rectangular bands located in the red and violet sides of the Ca II H and K lines. The counts in the reference bands of this channel were noted as N_{RV} . The other channel was used to measure the emission in the 1 Å rectangular bands centered at Ca II H or K lines. After completing the counts in either H or K lines, the relative instrumental fluxes $F_{\text{H}} = N_{\text{H}}/N_{\text{RV}}$ or $F_{\text{K}} = N_{\text{K}}/N_{\text{RV}}$ could be collected, where N_{H} and N_{K} are the counts in the 1 Å rectangular bands centered at Ca II H and K lines. Wilson (1968) employed $F = \frac{1}{2}(F_{\text{H}} + F_{\text{K}})$ to assess the emission of Ca II H and K lines collected by the HKP-1.

In view of the instrumental effects and certain limitations in the HKP-1, Vaughan et al. (1978) introduced the HKP-2, a four-channel spectrophotometer in 1977. The H and K channels collected the two 1.09 Å full width at half maximum (FWHM) triangular bandpasses in the line cores of Ca II H and K lines centered in the air wavelengths of 3968.47 and 3933.66 Å, respectively. In addition, the R and V channels measured the two 20 Å rectangular bandpasses on the red and violet sides of the Ca II H and K lines (wavelength ranges in air being 3991.07–4011.07 Å and 3891.07–3911.07 Å, respectively). The H, K, R and V channels are exposed sequentially and rapidly, with the exposure time of the H and K channels being eight times that of the R and V channels. To align the HKP-2 data with the HKP-1 data, Vaughan et al. (1978) performed a calibration of the HKP-2 data to match the HKP-1 data by

$$S_{\text{MWO}} = \alpha \cdot \frac{N_{\text{H}} + N_{\text{K}}}{N_{\text{R}} + N_{\text{V}}}, \quad (2)$$

where N_{H} , N_{K} , N_{R} and N_{V} are the counts in the H, K, R and V channels of HKP-2, respectively, and the scaling factor $\alpha = 2.4$ is applied to ensure the consistency of the results between HKP-2 and HKP-1 (Vaughan et al. 1978; Duncan et al. 1991).

Previous studies have utilized various bandpasses and definitions of chromospheric S index to calibrate their measurements from different instruments to the scale of MWO (Gray et al. 2003; Wright et al. 2004; Jenkins et al. 2011; Boudreaux et al. 2022). We discussed two typically definitions of the S index in Paper I, namely S_{rec} and S_{tri} , which are computed from the Ca II H and K lines using 1 Å rectangular bandpasses and 1.09 Å FWHM triangular bandpasses, respectively. As a conclusion, these two kinds of definition of S index is comparable for investigating the stellar chromospheric activity based on the Ca II H and K lines observed by LAMOST LRS. The S_{tri} is defined as

$$S_{\text{tri}} = \frac{\tilde{H}_{\text{tri}} + \tilde{K}_{\text{tri}}}{\tilde{R} + \tilde{V}}, \quad (3)$$

where \tilde{R} and \tilde{V} represent the mean fluxes in the 20 Å rectangular bandpasses centered in the vacuum wavelength of 4002.20 and 3902.17 Å, \tilde{H}_{tri} and \tilde{K}_{tri} are the mean fluxes in the 1.09 Å FWHM triangular bandpasses centered in the vacuum wavelength of 3969.59 and 3934.78 Å (Lovis et al. 2011; Zhang et al.

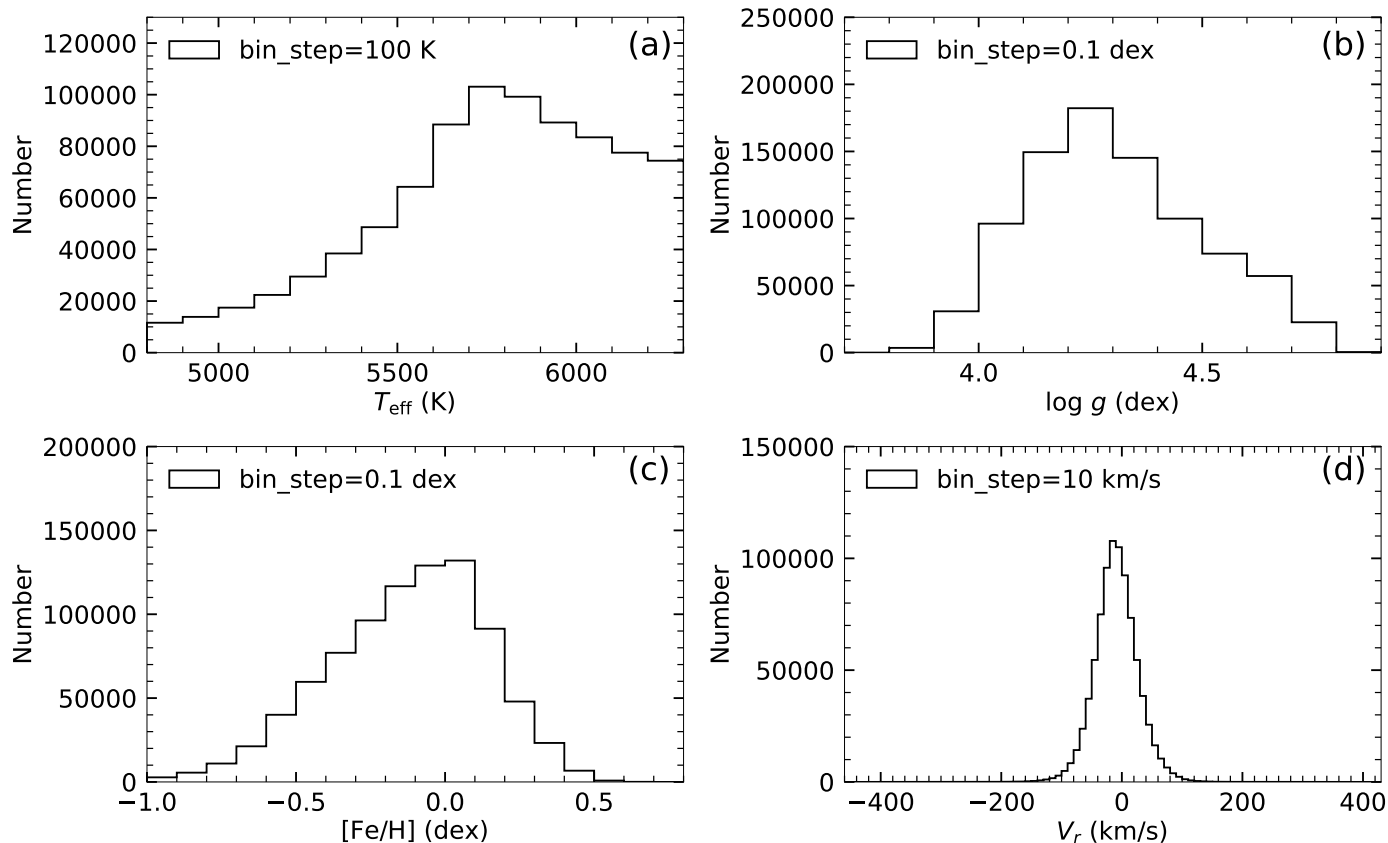


Fig. 3. Histograms of the (a) T_{eff} , (b) $\log g$, (c) $[\text{Fe}/\text{H}]$ and (d) V_r of the 861,505 solar-like stars employed in this work.

2022). Since the vacuum wavelength is adopted in LAOMST LRS spectra, the above vacuum wavelength values of the bandpasses center are converted from the corresponding wavelength values in air, see Paper I. The relationship between the value of vacuum wavelength and air wavelength is obtained from Ciddor (1996).

A denser and uniform distribution of wavelength is instrumental in integration of spectral flux. To estimate the mean fluxes in each bandpass, the step of spectral wavelength were linearly interpolated to 0.001 \AA . The wavelength shift caused by radial velocity could not be ignored, because the bandpasses used for calculating are narrow. We calibrate the spectral wavelength to the values in the rest frame before the calculation of chromospheric activity index. The pretreatment of wavelength based on V_r is introduced in Paper I.

In Paper I, 65 common stars were identified by cross-matching the database in that work and the S_{MWO} catalog of MWO in Duncan et al. (1991). A relationship between the S indexes of LAMOST and the S_{MWO} was introduced to calibrate the result of LAMOST to the scale of MWO. The relationship between the S_{tri} and S_{MWO} can be expressed by an exponential formula

$$S_{\text{MWO}} = e^{6.913 S_{\text{tri}} - 3.348}, \quad (4)$$

and the detailed technological process can be found in Paper I.

The histogram of $\sigma_{S_{\text{MWO}}}/S_{\text{MWO}}$ for stars with more than one observation is shown in Figure 4, where the $\sigma_{S_{\text{MWO}}}$ represent the standard deviation of S_{MWO} . For the majority of the samples (98.98%), the values of $\sigma_{S_{\text{MWO}}}/S_{\text{MWO}}$ are less than 0.1.

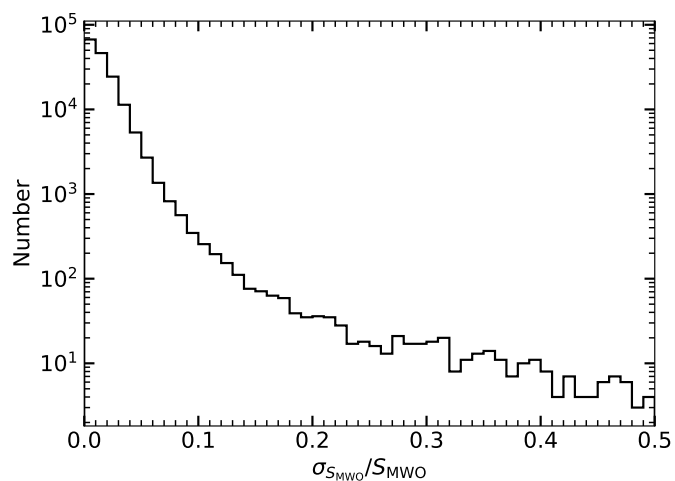


Fig. 4. Histogram of $\sigma_{S_{\text{MWO}}}/S_{\text{MWO}}$ for stars with more than one observation, where the $\sigma_{S_{\text{MWO}}}$ is the standard deviation of S_{MWO} .

3.2. Conversion of S_{MWO} to R_{HK}

In order to connect with physical quantity, the S_{MWO} can be described by the stellar surface fluxes as

$$S_{\text{MWO}} = 8\alpha \cdot \frac{\mathcal{F}_{\text{HK}}}{\mathcal{F}_{\text{RV}}}, \quad (5)$$

where \mathcal{F}_{HK} is the stellar surface flux in the 1.09 \AA FWHM H and K bands, and \mathcal{F}_{RV} represents the stellar surface flux in the 20 \AA R and V bands (Vaughan et al. 1978; Middelkoop 1982;

Rutten 1984; Hall et al. 2007; Mittag et al. 2013; Marvin et al. 2023). The constant 8 comes from the aforementioned different exposure times in HKP-2, and α represents the scaling factor in Equation 2 (Vaughan et al. 1978). The \mathcal{F}_{RV} mainly depends on the stellar atmospheric parameters, thus can be derived from empirical spectral library (e.g., Middelkoop 1982; Rutten 1984; Cincunegui et al. 2007; Suárez Mascareño et al. 2015; Astudillo-Defru et al. 2017; Lorenzo-Oliveira et al. 2018) or synthetic spectral library (e.g., Mittag et al. 2013; Pérez Martínez et al. 2014; Marvin et al. 2023). By combining the S_{MWO} with corresponding stellar continuum spectra of the empirical or synthetic spectral library, a new active index R_{HK} can be constructed as follows, which describes the emission of Ca II H and K lines more physically than S_{MWO} (e.g., Linsky et al. 1979; Middelkoop 1982; Rutten 1984; Noyes et al. 1984).

The stellar surface flux \mathcal{F}_{HK} in the 1.09 Å FWHM H and K bands can be normalised by the bolometric flux as

$$R_{\text{HK}} = \frac{\mathcal{F}_{\text{HK}}}{\sigma T_{\text{eff}}^4}, \quad (6)$$

where T_{eff} is the stellar effective temperature and $\sigma = 5.67 \times 10^{-5} \text{ erg cm}^{-2} \text{ s}^{-1} \text{ K}^{-4}$ is the Stefan-Boltzmann constant. R_{HK} is not related to the continuum flux around the Ca II H and K lines which is governed by the stellar effective temperature, thus it can be used to compare stars with different spectral types.

A widely used form of the relationship between S_{MWO} and R_{HK} can be expressed as

$$R_{\text{HK}} = K \cdot \sigma^{-1} \cdot 10^{-14} \cdot C_{\text{cf}} \cdot S_{\text{MWO}}, \quad (7)$$

where C_{cf} is the bolometric factor, and 10^{-14} is an arbitrary factor (Middelkoop 1982; Rutten 1984). The factor K is in unit of $\text{erg cm}^{-2} \text{ s}^{-1}$, which was introduced by Middelkoop (1982) to convert the relative flux F_{HK} (in arbitrary units)

$$F_{\text{HK}} = C_{\text{cf}} \cdot T_{\text{eff}}^4 \cdot 10^{-14} \cdot S_{\text{MWO}} \quad (8)$$

to stellar surface flux \mathcal{F}_{HK} by

$$\mathcal{F}_{\text{HK}} = K \cdot F_{\text{HK}}. \quad (9)$$

The factor C_{cf} in Equation 7 was derived by the pioneer studies of Middelkoop (1982) and Rutten (1984) (see e.g., Noyes et al. 1984; Henry et al. 1996; Wright et al. 2004; Hall et al. 2007; Egeland et al. 2017; Karoff et al. 2019; Sowmya et al. 2021; Gomes da Silva et al. 2021). Middelkoop (1982) first introduced and deduced the C_{cf} as a function of $B - V$ for main-sequence stars with $0.45 \leq B - V \leq 1.5$. Subsequently, Rutten (1984) broaden the C_{cf} to $0.3 \leq B - V \leq 1.6$ for FGK type main-sequence stars. To describe the chromospheric activity of M dwarf, Cincunegui et al. (2007) calibrated C_{cf} to the range $0.45 \leq B - V \leq 1.81$ for stars with spectral type ranging from F6 to M5, and Suárez Mascareño et al. (2015) calibrated the C_{cf} in the range of $0.4 \leq B - V \leq 1.9$. On the other hand, Astudillo-Defru et al. (2017) derived the C_{cf} in the range of $0.54 \leq B - V \leq 1.90$ to include the M dwarf, and they prefer the forms of C_{cf} described by the color indexes $I - K$ and $V - K$. Lorenzo-Oliveira et al. (2018) calibrated the C_{cf} to a function of T_{eff} .

The preceding researches of C_{cf} are based on empirical method, which can also be obtained from synthetic spectral library. The PHOENIX model atmospheres were utilized by Mittag et al. (2013) to obtain \mathcal{F}_{RV} for main-sequence stars, and the relation between \mathcal{F}_{RV} and $B - V$ is given as

$$\log \frac{\mathcal{F}_{\text{RV}}}{19.2} = 8.33 - 1.79(B - V), \quad (10)$$

where $0.44 \leq B - V \leq 1.6$, and the constant 19.2 is equal to the scaling factor 8α in Equation 5. \mathcal{F}_{RV} is comparable with C_{cf} , which can be transfer to C_{cf} through

$$C_{\text{cf}} = \frac{\mathcal{F}_{\text{RV}}}{8\alpha \cdot K \cdot T_{\text{eff}}^4 \cdot 10^{-14}}, \quad (11)$$

based on Equations 5, 8 and 9. Through matching the PHOENIX spectral library with observed spectra, Pérez Martínez et al. (2014) introduced a quadratic formula of C_{cf} within $0.44 \leq B - V \leq 1.33$ for luminosity classes V and IV with $\log g$ between 5.0 and 3.5 dex. Marvin et al. (2023) derived the C_{cf} as a fifth-order function of T_{eff} based on the synthetic spectral library of PHOENIX.

The C_{cf} in different researches described above generally can be expressed with a polynomial

$$\log C_{\text{cf}}(X) = \sum_{i=0}^5 C_i X^i, \quad (12)$$

where X represents $B - V$ or T_{eff} , and C_i ($i=0, \dots, 5$) are the corresponding coefficients which are presented in Table 1.

The S_{MWO} can be derived from observed spectra, and C_{cf} can be estimated by stellar color index or T_{eff} as described above. The remaining coefficient in Equation 7 to be determined is the factor K . Middelkoop (1982) deduced the $K = (0.76 \pm 0.11) \times 10^6 \text{ erg cm}^{-2} \text{ s}^{-1}$ based on the investigation of Linsky et al. (1979), thus $K \cdot \sigma^{-1} \cdot 10^{-14} = 1.34 \times 10^{-4}$, which is frequently adopted in the relevant works (e.g., Cincunegui et al. 2007; Pérez Martínez et al. 2014; Suárez Mascareño et al. 2015; Boro Saikia et al. 2018; Gomes da Silva et al. 2021). Rutten (1984) derived $K = (1.29 \pm 0.19) \times 10^6 \text{ erg cm}^{-2} \text{ s}^{-1}$ based on the solar S index $S_{\text{MWO}, \odot} = 0.160$ (Oranje 1983) and the color index of the Sun $(B - V)_{\odot} = 0.665$ (Hardorp 1980). Additionally, Hall et al. (2007) conducted a recalibration of the K value, obtaining a result of $(1.07 \pm 0.13) \times 10^6 \text{ erg cm}^{-2} \text{ s}^{-1}$. They pointed out that the discrepancy between their result and the K value reported by Rutten (1984) is mainly due to the adoption of a different solar $B - V$ value, which they took to be 0.642 (Cayrel de Strobel 1996). $K \cdot \sigma^{-1} \cdot 10^{-14} = 1.887 \times 10^{-4}$ is gradually adopted in recent works (e.g., Astudillo-Defru et al. 2017; Melbourne et al. 2020; Boudreaux et al. 2022; Marvin et al. 2023).

In this work, the value of R_{HK} derived from the method in the classic literature for the LRS spectra is denoted as $R_{\text{HK,classic}}$, which is calculated by utilizing the C_{cf} from Rutten (1984) (row 2 in Table 1) and $K = 0.76 \times 10^6 \text{ erg cm}^{-2} \text{ s}^{-1}$ from Middelkoop (1982). Since the value of $B - V$ is needed for the estimation of $R_{\text{HK,classic}}$, we use the relation between T_{eff} and $B - V$ introduced in Noyes et al. (1984) to transform T_{eff} to $B - V$ when calculating $R_{\text{HK,classic}}$, which is based on the research of Johnson (1966). The transformation is given by

$$\log T_{\text{eff}} = 3.908 - 0.234(B - V), \quad (13)$$

in the range $0.4 < B - V < 1.4$.

Based on Equations 5 and 6, we can express R_{HK} by S_{MWO} and \mathcal{F}_{RV} as

$$R_{\text{HK}} = \frac{S_{\text{MWO}} \cdot \mathcal{F}_{\text{RV}}}{8\alpha} \cdot \frac{1}{\sigma T_{\text{eff}}^4}. \quad (14)$$

As described above, recent studies have demonstrated that the PHOENIX model is a useful tool for deriving the stellar surface flux \mathcal{F}_{RV} . In this work, besides $R_{\text{HK,classic}}$ we also utilize the spectral library of PHOENIX to estimate \mathcal{F}_{RV} , and then derive R_{HK}

Table 1. Coefficients for the $\log C_{\text{cf}}$ expression in Equation 12 in different researches.

Source	C_0	C_1	C_2	C_3	C_4	C_5	Valid Range of $B - V$ or T_{eff}
(1)	-0.47	2.84	-3.91	1.13	/	/	$0.45 \leq B - V \leq 1.5$
(2)	0.24	0.43	-1.33	0.25	/	/	$0.3 \leq B - V \leq 1.6$
(3)	0.8	-1.41	0.55	-0.33	/	/	$0.45 \leq B - V \leq 1.81$
(4)	0.66	-1.11	/	/	/	/	$0.44 \leq B - V \leq 1.33$
(5)	0.668	-1.270	0.645	-0.443	/	/	$0.4 \leq B - V \leq 1.9$
(6)	0.669	-0.972	0.109	-0.203	/	/	$0.54 \leq B - V \leq 1.90$
(7)	-7.31	2.25×10^{-3}	-1.70×10^{-7}	/	/	/	$4350 \leq T_{\text{eff}} \leq 6500 \text{ K}$
(8)	-29.679	0.026864	-1.0268×10^{-5}	1.9866×10^{-9}	-1.9017×10^{-13}	7.1548×10^{-18}	$2300 \leq T_{\text{eff}} \leq 7200 \text{ K}$

References. (1) Middelkoop (1982); (2) Rutten (1984) (used for the calculation of $R_{\text{HK,classic}}$); (3) Cincunegui et al. (2007); (4) Pérez Martínez et al. (2014); (5) Suárez Mascareño et al. (2015); (6) Astudillo-Defru et al. (2017); (7) Lorenzo-Oliveira et al. (2018); (8) Marvin et al. (2023).

through Equation 14, denoted as $R_{\text{HK,PHOENIX}}$. Because the detailed stellar atmospheric parameters (T_{eff} , $\log g$ and $[\text{Fe}/\text{H}]$) are available for LAMOST (see Section 2), and the \mathcal{F}_{RV} values estimated from the PHOENIX synthetic spectra library are related to these stellar parameters, we evaluate the values of $R_{\text{HK,PHOENIX}}$ taking these parameters into account.

Husser et al. (2013) published a high-resolution synthetic spectral library³ based on the version 16 of the PHOENIX model atmospheres. The stellar atmospheric parameter space of their library covers $2300 \leq T_{\text{eff}} \leq 12000 \text{ K}$, $0.0 \leq \log g \leq 6.0 \text{ dex}$ and $-4.0 \leq [\text{Fe}/\text{H}] \leq 1.0 \text{ dex}$. In Lançon et al. (2021), a comparison between the PHOENIX synthetic spectra library and empirical spectra was conducted, and their results show that the spectra of Husser et al. (2013) exhibit good consistency with the empirical spectra in the effective temperature range down to about 4000 K. Considering the stellar parameters space of the LAMOST LRS spectra of solar-like stars used in this work as described in Section 2, we utilize the spectra in Husser et al. (2013) within the range of $4800 \leq T_{\text{eff}} \leq 6300 \text{ K}$, $3.5 \leq \log g \leq 5.0 \text{ dex}$ and $-1.0 \leq [\text{Fe}/\text{H}] \leq 1.0 \text{ dex}$. A total of 320 high-resolution synthetic spectra in this parameter range are collected to calculate the value of \mathcal{F}_{RV} . We fitted $\log \mathcal{F}_{\text{RV}}$ by a ternary quadratic polynomial

$$\begin{aligned} \log \mathcal{F}_{\text{RV}} = & -138.7639 + 70.3122X + 0.3893Y - 2.3216Z, \\ & -0.0806X \cdot Y - 0.5840X \cdot Z + 0.0124Y \cdot Z \quad (15) \\ & -8.2986X^2 - 0.01242Y^2 - 0.0351Z^2, \end{aligned}$$

where the X , Y and Z represent $\log T_{\text{eff}}$, $\log g$ and $[\text{Fe}/\text{H}]$, respectively. The fitting coefficients are calculated by the nonlinear least square method through the python module `curve_fit` of `scipy.optimize` (Virtanen et al. 2020). In Figure 5, we present the relationships between \mathcal{F}_{RV} and $B - V$ (or T_{eff}) adopted in different researches. The \mathcal{F}_{RV} values of the PHOENIX spectra used for deriving Equation 15 are exhibited with the gray circles. The black solid line in Figure 5 is derived from Equation 15 with $\log g = 4.44 \text{ dex}$ and $[\text{Fe}/\text{H}] = 0.0 \text{ dex}$ (solar parameters). It can be seen from Figure 5 that the results of Hall et al. (2007) ($K = 1.07 \times 10^6 \text{ erg cm}^{-2} \text{ s}^{-1}$ and C_{cf} taken from Middelkoop (1982)) using empirical spectra library is relatively close to the results calculated from the PHOENIX synthetic spectral library.

The $\mathcal{F}_{\text{HK,PHOENIX}}$ value of the Sun is estimated to be $(2.423 \pm 0.007) \times 10^6 \text{ erg cm}^{-2} \text{ s}^{-1}$, which is calculated by Equations 5 and 15 with $T_{\text{eff}} = 5777 \text{ K}$, $\log g = 4.44 \text{ dex}$, $[\text{Fe}/\text{H}] = 0.0 \text{ dex}$ and $S_{\text{MWO},\odot} = 0.1694 \pm 0.0005$. The selected values of solar T_{eff} and $\log g$ are following Ramírez et al. (2012). The $S_{\text{MWO},\odot}$ is

³ <http://phoenix.astro.physik.uni-goettingen.de/>

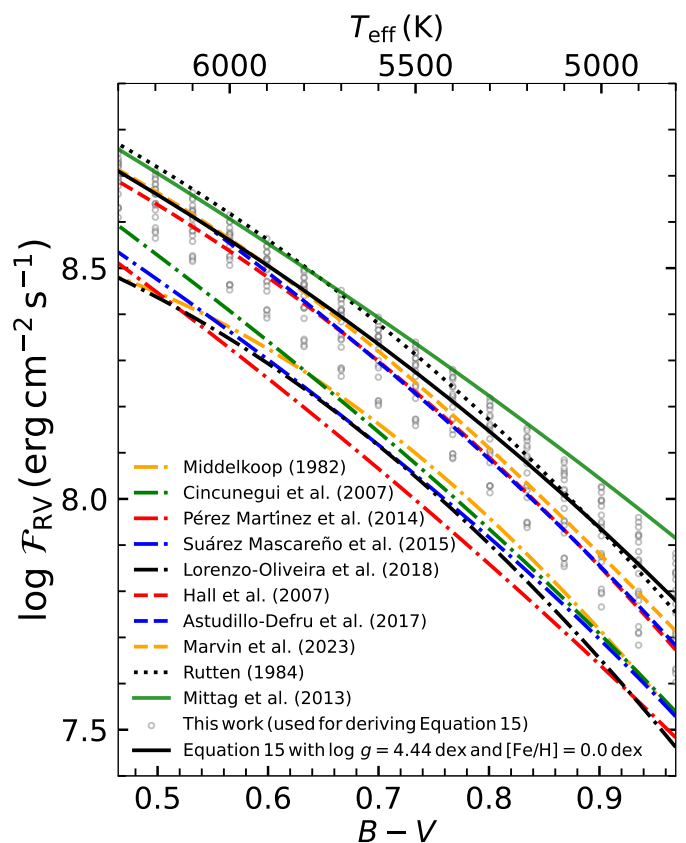


Fig. 5. Relations between $\log \mathcal{F}_{\text{RV}}$ and $B - V$ (or T_{eff}) adopted in different researches. For the works using C_{cf} and K instead of \mathcal{F}_{RV} , the values of \mathcal{F}_{RV} are estimated by Equation 11. The dashed-dotted, dashed and dotted lines represent the results using $K = 0.76 \times 10^6$, 1.07×10^6 and $1.29 \times 10^6 \text{ erg cm}^{-2} \text{ s}^{-1}$, respectively. The gray circles represent the \mathcal{F}_{RV} values estimated from the PHOENIX model used for deriving Equation 15. The black solid line is derived from Equation 15 with $\log g = 4.44 \text{ dex}$ and $[\text{Fe}/\text{H}] = 0.0 \text{ dex}$.

the mean value of the solar S index which is obtained from the MWO HKP-2 measurements by Egeland et al. (2017). The solar \mathcal{F}_{HK} values estimated by Oranje (1983), Hall et al. (2007) and Mittag et al. (2013) are $(2.17 \pm 0.32) \times 10^6$, $(2.12 \pm 0.25) \times 10^6$ and $(2.47 \pm 0.10) \times 10^6 \text{ erg cm}^{-2} \text{ s}^{-1}$, respectively. Our evaluation of $\mathcal{F}_{\text{HK},\odot}$ value is consistent with those values estimated in previous investigations with a slight deviation. The deviation may originate from the different spectral fluxes in the PHOENIX

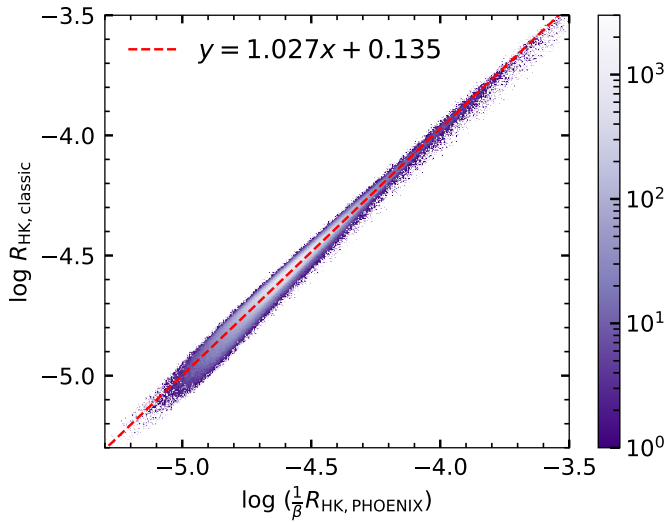


Fig. 6. Scatter diagram between $\log(\frac{1}{\beta}R_{\text{HK,PHOENIX}})$ and $\log R_{\text{HK,classic}}$ for the LAMOST LRS spectra of solar-like stars used in this work. The color scale indicates the density of data points. The dashed line represents the linear fit between $\log(\frac{1}{\beta}R_{\text{HK,PHOENIX}})$ and $\log R_{\text{HK,classic}}$.

model, the different choices of solar atmospheric parameters, and the different value of $S_{\text{MWO},\odot}$. As a result, the values of $R_{\text{HK,PHOENIX}}$ are relatively higher than $R_{\text{HK,classic}}$, with a boost factor $\beta = 1.6$. Figure 6 displays a comparison between the values of $\log(\frac{1}{\beta}R_{\text{HK,PHOENIX}})$ and $\log R_{\text{HK,classic}}$ for the LAMOST LRS spectra of solar-like stars used in this work. The correlation between them can be fitted by a linear formula

$$\log R_{\text{HK,classic}} = 1.027 \log\left(\frac{1}{\beta}R_{\text{HK,PHOENIX}}\right) + 0.135. \quad (16)$$

3.3. Derivation of the Bolometric and Photospheric Calibrated Chromospheric Activity Index R'_{HK}

The emission flux of Ca II H and K lines is known as comprising the fluxes of stellar photosphere and chromosphere (Hartmann et al. 1984; Noyes et al. 1984). To acquire a purer chromospheric activity index, we should subtract the photospheric contribution from R_{HK} . The photospheric and bolometric calibrated chromospheric activity index R'_{HK} (Hartmann et al. 1984; Noyes et al. 1984) is defined as

$$R'_{\text{HK}} = R_{\text{HK}} - R_{\text{phot}}, \quad (17)$$

where R_{HK} has been described and derived in Section 3.2, and R_{phot} represents the photospheric contribution which is the ratio between the photospheric flux and the bolometric flux

$$R_{\text{phot}} = \frac{\mathcal{F}_{\text{phot}}}{\sigma T_{\text{eff}}^4}. \quad (18)$$

R_{phot} can be derived from empirical spectral library (e.g., Hartmann et al. 1984; Noyes et al. 1984; Suárez Mascareño et al. 2015; Lorenzo-Oliveira et al. 2018) or synthetic spectral library (e.g., Mittag et al. 2013; Astudillo-Defru et al. 2017; Marvin et al. 2023). The value of $\log R_{\text{phot}}$ in the literature that can be expressed by the polynomial form

$$\log R_{\text{phot}} = \sum_{i=0}^5 P_i X^i \quad (19)$$

are presented in Table 2. In Equation 19, X represents $B - V$ or T_{eff} and the P_i ($i=1, \dots, 5$) are the coefficients of the polynomial which are given in Table 2.

Noyes et al. (1984) distilled the result of Hartmann et al. (1984) and expressed the relation between $\log R_{\text{phot}}$ and $B - V$ via a cubic polynomial

$$\log R_{\text{phot}} = -4.898 + 1.918(B - V)^2 - 2.893(B - V)^3, \quad (20)$$

for the main-sequence stars with $B - V > 0.44$ (see first row of Table 2). They noted that R_{phot} becomes negligible for the case of $B - V \gtrsim 1.0$. This expression of R_{phot} in Equation 20 was widely adopted to derive R'_{HK} in the majority of researches (e.g., Henry et al. 1996; Wright et al. 2004; Gray et al. 2006; Gomes da Silva et al. 2021), while a simpler linear form of $\log R_{\text{phot}}$ is also available (used in Cincunegui et al. 2007). By cross-match 72 stars with Noyes et al. (1984), Lorenzo-Oliveira et al. (2018) fitted the $\log R_{\text{phot}}$ into a formula of T_{eff}

$$\log R_{\text{phot}} = -4.78845 - \frac{3.70700}{1 + (T_{\text{eff}}/4598.92)^{17.527}}, \quad (21)$$

for stars in the range of $4350 \leq T_{\text{eff}} \leq 6500$ K. Based on the inactive stars observed by HARPS spectra, Suárez Mascareño et al. (2015) empirically fitted the R_{phot} for the main-sequence star in the range $0.4 \lesssim B - V \lesssim 1.9$, which expressed by an exponential function

$$R_{\text{phot}} = 1.48 \times 10^{-4} \cdot e^{-4.3658(B-V)}. \quad (22)$$

Mittag et al. (2013) adopted the synthetic spectra of PHOENIX to deduce the photospheric flux $\mathcal{F}_{\text{phot}}$, which is expressed by a linear equation for main-sequence star in the range of $0.44 \leq B - V < 1.28$ as

$$\log \mathcal{F}_{\text{phot}} = 7.49 - 2.06(B - V), \quad (23)$$

which can be converted to R_{phot} by Equation 18.

Astudillo-Defru et al. (2017) derived the R_{phot} in the range of $0.54 \leq B - V \leq 1.90$ based on the BT-Settl model (Allard 2014). Besides, Marvin et al. (2023) employed the PHOENIX model to deduce a fifth-order equation that expresses the $\log R_{\text{phot}}$ as a function of T_{eff} . For the same stellar $B - V$ or T_{eff} value, the values of R_{phot} deduced by synthetic spectra in Mittag et al. (2013), Astudillo-Defru et al. (2017) and Marvin et al. (2023) are generally higher than the empirical calibration of Noyes et al. (1984). Marvin et al. (2023) thus introduced an offset 0.4612 to scale their result to Noyes et al. (1984).

Same as R_{HK} described in Section 3.2, we present two kinds of estimations of R'_{HK} , denoted as $R'_{\text{HK,classic}}$ and $R'_{\text{HK,PHOENIX}}$, respectively. $R'_{\text{HK,classic}}$ is calculated using $R_{\text{HK,classic}}$ and the photospheric contribution derived from Equation 20 with $B - V$ estimated from Equation 13, while $R'_{\text{HK,PHOENIX}}$ is computed based on $R_{\text{HK,PHOENIX}}$ and the photospheric contribution $R_{\text{phot,PHOENIX}}$ estimated as follows.

Because the values of $R_{\text{HK,PHOENIX}}$ are approximately β times larger than the values of $R_{\text{HK,classic}}$, we introduce a β -coefficient to scale $R_{\text{phot,classic}}$ to $R_{\text{phot,PHOENIX}}$ and the corresponding $\log R_{\text{phot,PHOENIX}}$ can be expressed by

$$\begin{aligned} \log R_{\text{phot,PHOENIX}} &= \log(\beta \cdot R_{\text{phot,classic}}) \\ &= -4.694 + 1.918(B - V)^2 - 2.893(B - V)^3, \end{aligned} \quad (24)$$

for $B - V > 0.44$. In Figure 7, we present the relations between $\log R_{\text{phot}}$ and $B - V$ (or T_{eff}) adopted in different researches. As

Table 2. Coefficients for the $\log R_{\text{phot}}$ expression in Equation 19 in different researches.

Source	P_0	P_1	P_2	P_3	P_4	P_5	Valid Range of $B - V$ or T_{eff}
(1)	-4.898	0	1.918	-2.893	/	/	$0.44 < B - V$
(2)	-3.749	-1.036	-0.026	-0.045	/	/	$0.54 \leq B - V \leq 1.90$
(3)	-37.550	0.032131	-1.3177×10^{-5}	2.7133×10^{-9}	-2.7466×10^{-13}	1.0887×10^{-17}	$2300 \leq T_{\text{eff}} \leq 7200 \text{ K}$

References. (1) Noyes et al. (1984) (used for the calculation of $R'_{\text{HK,classic}}$); (2) Astudillo-Defru et al. (2017); (3) Marvin et al. (2023);

discussed above, the $R_{\text{phot,PHOENIX}}$ is scaled from the results of Noyes et al. (1984) using a scale factor β related to the method based on the PHOENIX model. Hence, the red solid curve in Figure 7 differs from those obtained in Mittag et al. (2013) and Marvin et al. (2023).

Since the detailed stellar atmospheric parameters (T_{eff} , $\log g$ and $[\text{Fe}/\text{H}]$) are available for LAMOST, we estimate the $B - V$ in Equation 24 by considering not only T_{eff} , but also the stellar atmospheric parameters $\log g$ and $[\text{Fe}/\text{H}]$. Based on the InfraRed Flux Method, Casagrande et al. (2010) found that there is very little dependence of $B - V$ on $\log g$ and provided a relation between T_{eff} , $B - V$, and $[\text{Fe}/\text{H}]$, with $B - V$ and $[\text{Fe}/\text{H}]$ in the range of $0.18 \leq B - V \leq 1.29$ and $-5.0 \leq [\text{Fe}/\text{H}] \leq 0.4$ dex. We examine the extendability of the $[\text{Fe}/\text{H}]$ upper boundary and still employ the relation to obtain the $B - V$ for the small amount of spectra with $[\text{Fe}/\text{H}]$ slightly exceeding 0.4 dex. After obtaining $B - V$ from T_{eff} and $[\text{Fe}/\text{H}]$, we then estimate the photospheric contribution $R_{\text{phot,PHOENIX}}$ based on Equation 24. Because both the $R_{\text{HK,PHOENIX}}$ and $R_{\text{phot,PHOENIX}}$ are about β times higher than the corresponding classic indexes, to be consistent with classic studies, we calculated the $R'_{\text{HK,PHOENIX}}$ by

$$R'_{\text{HK,PHOENIX}} = \frac{1}{\beta} (R_{\text{HK,PHOENIX}} - R_{\text{phot,PHOENIX}}). \quad (25)$$

In Figure 8, we present a comparison between the values of the two indexes $\log R'_{\text{HK,PHOENIX}}$ and $\log R'_{\text{HK,classic}}$ for the LAMOST LRS spectra of solar-like stars studied in this work. As shown in Figure 8, there exists a linear correlation between these two quantities, the fitting formula is

$$\log R'_{\text{HK,classic}} = 0.999 \log R'_{\text{HK,PHOENIX}} + 0.009. \quad (26)$$

Egeland et al. (2017) estimated the average value of $\log R'_{\text{HK},\odot}$ as -4.9427 ± 0.0072 based on the $S_{\text{MWO},\odot}$ in the 15–24 solar cycle and $(B - V)_{\odot} = 0.653 \pm 0.003$. Taking $T_{\text{eff}} = 5777 \text{ K}$, $\log g = 4.44$ dex, $[\text{Fe}/\text{H}] = 0.0$ dex and the same solar $B - V$, we can obtain the $\log R'_{\text{HK,PHOENIX}} = -4.9599 \pm 0.0051$ for the Sun.

3.4. Estimation of the Uncertainty of Chromospheric Activity Indexes

We estimated the uncertainties of $\log R_{\text{HK,classic}}$, $\log R'_{\text{HK,classic}}$, $\log R_{\text{HK,PHOENIX}}$, and $\log R'_{\text{HK,PHOENIX}}$ with the Monte Carlo error propagation. Because the $\log R_{\text{HK,PHOENIX}}$ values are calculated by Equation 14, the uncertainties of $\log R_{\text{HK,PHOENIX}}$ are yielded from the uncertainties of S_{MWO} and \mathcal{F}_{RV} . The uncertainties of $\log R_{\text{HK,classic}}$ predominantly arise from the uncertainties of S_{MWO} and C_{cf} as presented in Equation 7. As illustrated in Paper I, we estimated the uncertainties of S_{MWO} by considering the impact of the uncertainties of the spectral flux, the discretization in spectral data, and the uncertainty of radial velocity. Regarding the uncertainties of \mathcal{F}_{RV} , it is affected by the uncertainties of stellar atmospheric parameters T_{eff} , $\log g$ and $[\text{Fe}/\text{H}]$ due to

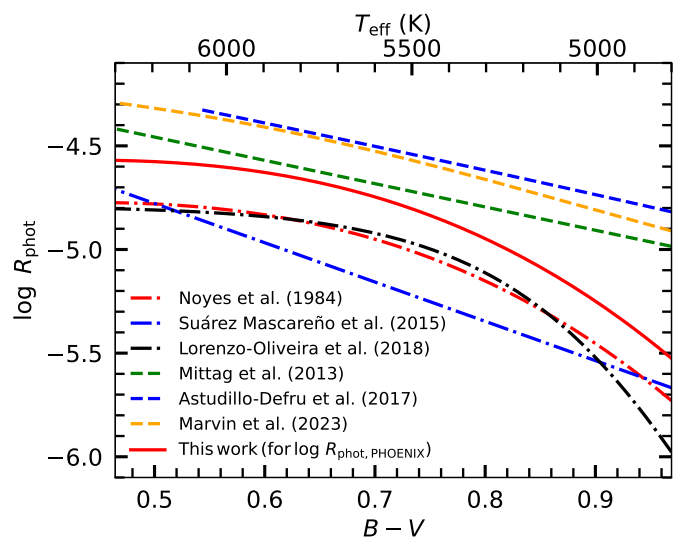


Fig. 7. Relations between $\log R_{\text{phot}}$ and $B - V$ (or T_{eff}) adopted in different researches. The formulas derived from empirical and synthetic spectral libraries in the literature are indicated by dashed-dotted and dashed lines respectively. The formula of $\log R_{\text{phot,PHOENIX}}$ adopted in this work is indicated by the red solid line.

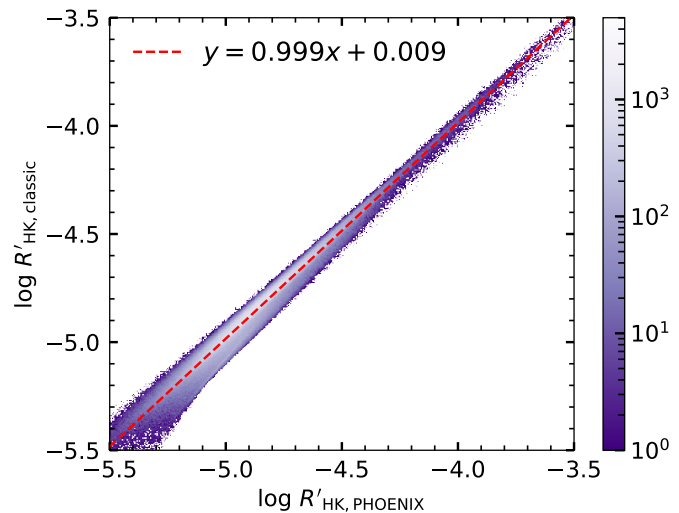


Fig. 8. Scatter diagram between $\log R'_{\text{HK,PHOENIX}}$ and $\log R'_{\text{HK,classic}}$ for the LAMOST LRS spectra of solar-like stars studied in this work. The color scale represents the density of data points. The dashed line is the linear fit between $\log R'_{\text{HK,PHOENIX}}$ and $\log R'_{\text{HK,classic}}$.

Equation 15. Since we calculate the value of C_{cf} through the $B - V$ value derived from Equation 13, the uncertainties of C_{cf} are influenced by the uncertainties of $B - V$ which is propagated from the uncertainties of T_{eff} .

Figure 9(a) illustrates the histograms of the uncertainties of $\log S_{\text{MWO}}$, $\log C_{\text{cf}}$, $\log R_{\text{HK,classic}}$, $\log R_{\text{phot,classic}}$ and $\log R'_{\text{HK,classic}}$, while Figure 9(b) shows the uncertainties for $\log S_{\text{MWO}}$, $\log \mathcal{F}_{\text{RV}}$, $\log R_{\text{HK,PHOENIX}}$, $\log R_{\text{phot,PHOENIX}}$ and $\log R'_{\text{HK,PHOENIX}}$. As shown in Figure 9, the uncertainties of $\log R_{\text{HK,PHOENIX}}$ and $\log R_{\text{HK,classic}}$ are both primarily governed by the uncertainties of S_{MWO} . The uncertainties of $\log S_{\text{MWO}}$, $\log R_{\text{HK,classic}}$, $\log R'_{\text{HK,classic}}$, $\log R_{\text{HK,PHOENIX}}$ and $\log R'_{\text{HK,PHOENIX}}$ are distributed around 0.030, 0.030, 0.065, 0.030 and 0.065 respectively.

4. Results and Discussion

4.1. Stellar Chromospheric Activity Database

In Section 3, we investigate the stellar chromospheric activity through two kinds of methods. The chromospheric activity parameters derived from the method in the classic literature are denoted with `classic`, while those derived from the method based on the PHOENIX model are denoted with `PHOENIX`. We provide the database of chromospheric activity parameters for 1,122,495 LAMOST LRS spectra of solar-like stars, which is available at <https://doi.org/10.5281/zenodo.8378849> (compiled in a CSV format file: `CaIIHK_Activity_Indexes_LAMOST_DR8_LRS.csv`). The database mainly includes the chromospheric activity parameters S_{tri} , S_{MWO} , $R_{\text{HK,classic}}$, $R'_{\text{HK,classic}}$, $R_{\text{HK,PHOENIX}}$ and $R'_{\text{HK,PHOENIX}}$, as well as their uncertainties. The columns in the catalog of the database are presented in Table 3.

The $\log R'_{\text{HK,classic}}$ and $\log R'_{\text{HK,PHOENIX}}$ values of 743 and 821 spectra, respectively, are not available (recorded as '-9999' in the database). One of the reason is the value of stellar parameters exceeds the valid range of the empirical formula of R_{phot} (0 and 13 spectra for `classic` and `PHOENIX`, respectively). The other reason is that the estimated value of photospheric contribution is large than the value of R_{HK} for very few spectra (743 and 808 spectra for `classic` and `PHOENIX`, respectively). This situation would occur because the photospheric contributions are determined empirically, leading to overestimations for some stars; or there are uncertainties in the evaluation of R_{HK} . These spectra are not involved in the subsequent discussion. In Sections 3.2 and 3.3, we have performed a comparison between $\log R_{\text{HK,classic}}$ and $\log R_{\text{HK,PHOENIX}}$, and between $\log R'_{\text{HK,classic}}$ and $\log R'_{\text{HK,PHOENIX}}$. The results indicate that $\log R_{\text{HK,PHOENIX}}$ and $\log R'_{\text{HK,PHOENIX}}$ are approximately linearly correlated with $\log R_{\text{HK,classic}}$ and $\log R'_{\text{HK,classic}}$, respectively (see Figures 6 and 8). In the next subsection, we discuss the distribution of chromospheric activity primarily based on $R_{\text{HK,PHOENIX}}$ and $R'_{\text{HK,PHOENIX}}$.

4.2. Distribution of Chromospheric Activity Index

Among the 1,122,495 LAMOST LRS spectra of solar-like stars, there are 861,505 stars with 'gaia_source_id' available in LAMOST LRS AFGK Catalog. In this section, we investigate the distribution of chromospheric activity index based on these stars. If a star is recorded more than once in our dataset, we use the median values of the chromospheric activity parameters from the multiple observed spectra. In Paper I, we have calibrated the S index of LAMOST to S_{MWO} , and we also compare the R'_{HK} with the results in the literatures, as illustrated in Appendix B. There is an approximate consistency between our R'_{HK} values and those from other instruments for the common targets.

In Figure 10, we display the distribution of $\log R_{\text{HK,PHOENIX}}$ with T_{eff} for the 861,505 solar-like stars. The solar value of $\log R_{\text{HK,PHOENIX}}$ (-4.416 ± 0.001) is displayed in Figure 10 with a '*' symbol, which is calculated by Equation 6 with the solar $\mathcal{F}_{\text{HK,PHOENIX}} = (2.423 \pm 0.007) \times 10^6 \text{ erg cm}^{-2} \text{ s}^{-1}$ given in Section 3.2.

It is not surprising that the distribution trend of $\log R_{\text{HK,PHOENIX}}$ shows a clear correlation with T_{eff} . Although the $R_{\text{HK,PHOENIX}}$ is the bolometric calibration of the surface flux, the photospheric contribution related to stellar spectral types is still contained. As mentioned in Section 3.3, it is necessary to further remove the contribution of photosphere to obtain $R'_{\text{HK,PHOENIX}}$. The histograms of the $\log R'_{\text{HK,PHOENIX}}$ values are exhibited in Figures 11(a) and (b) in linear-scale and logarithmic-scale vertical axes, respectively. The peak of the distribution is at about -4.90. This peak value is close to the solar $\log R'_{\text{HK,PHOENIX}} = -4.9599$ as given in Section 3.3.

The Vaughan-Preston gap (VP gap, Vaughan & Preston 1980), known as the bimodal distribution of chromospheric activity, is not observed in Figure 11. The separation of $\log R'_{\text{HK}}$ values between active and inactive stars may suggest the existence of different dynamo mechanisms (Vaughan & Preston 1980; Noyes et al. 1984; Henry et al. 1996; Jenkins et al. 2006; Gray et al. 2006; Gomes da Silva et al. 2021). Boro Saikia et al. (2018) investigated a global sample of 4451 cool stars from high-resolution HARPS spectra and concluded that the VP gap is not pronounced. A significant proportion of the stars have intermediate activity levels around $\log R'_{\text{HK}} = -4.75$ in Boro Saikia et al. (2018). In contrast, the bimodal distribution of chromospheric activity in Gomes da Silva et al. (2021) is relatively significant, based on 1674 F-, G- and K-type stars from the HARPS sample. Gray et al. (2006) and Hinkel et al. (2017) proposed that the VP gap tends to appear for stars with $[\text{Fe}/\text{H}]$ greater than -0.2, which is inflexible for stars in this work. The VP gap is also influenced by the rotation rate (e.g. Noyes et al. 1984; Rutten 1987), and the relationship between rotation and stellar chromospheric activity in LAMOST samples will be investigated in the future. Vaughan & Preston (1980) suggested that the VP gap might originate from different dynamo mechanisms or statistical bias. The absence of VP gap in the distribution of chromospheric activity for our solar-like stars could be attributed to three possible factors: 1) a gradual diminishing of chromospheric activity during the evolution of solar-like stars; 2) the influence of different stellar properties on the bimodal distribution of the chromospheric activity within our samples, which should be explored in more detail in the future, or 3) the loss of some information in the spectral profile due to the limited resolution of LAMOST LRS spectra (Jenkins et al. 2011).

We display the distributions of $\log R'_{\text{HK,PHOENIX}}$ with T_{eff} , $\log g$ and $[\text{Fe}/\text{H}]$ in Figures 12(a), (b) and (c), respectively. To show the trends of $\log R'_{\text{HK,PHOENIX}}$ with these stellar atmospheric parameters, the $\log R'_{\text{HK,PHOENIX}}$ values are homogeneously segregated into equal-width bins for $4800 < T_{\text{eff}} < 6300 \text{ K}$, $3.9 < \log g < 4.8 \text{ dex}$ and $-1.0 < [\text{Fe}/\text{H}] < 0.6 \text{ dex}$ with steps of 50 K, 0.1 dex and 0.1 dex, respectively; and the fitted median values of the $\log R'_{\text{HK,PHOENIX}}$ in each bin with T_{eff} , $\log g$ and $[\text{Fe}/\text{H}]$ are marked by the black dashed lines in Figure 12. The formulas of these fitted trends are expressed by the following quadratic polynomials

$$\log R'_{\text{HK,PHOENIX}} = 4.367 - 3.397 \times 10^{-3} T_{\text{eff}} + 3.094 \times 10^{-7} T_{\text{eff}}^2, \quad (27)$$

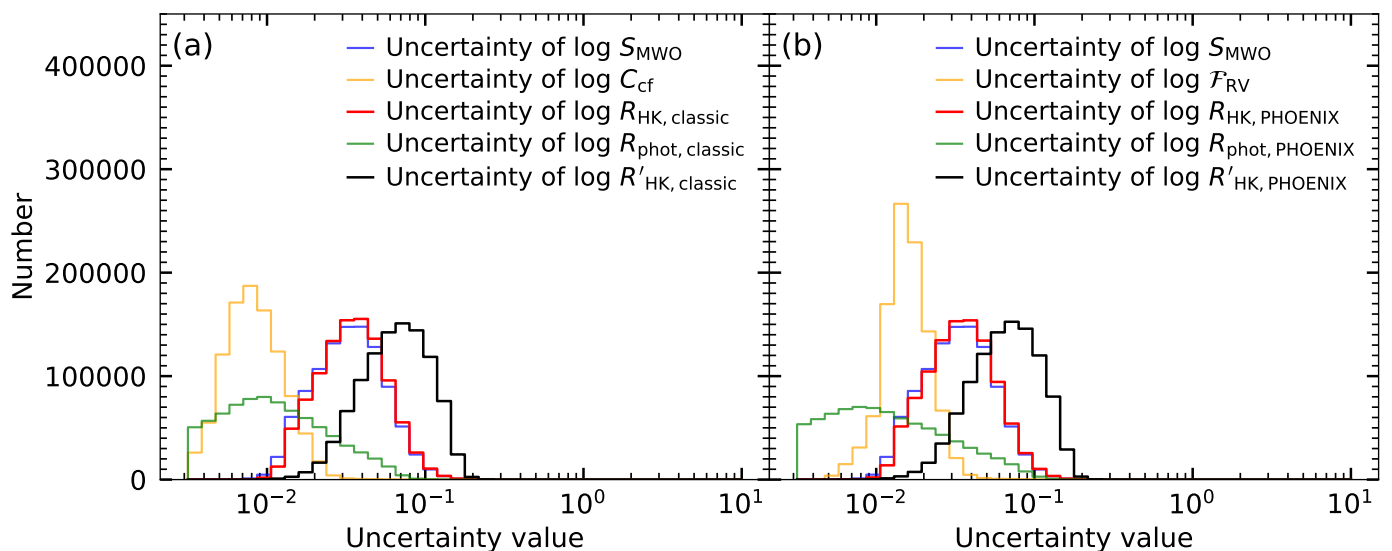


Fig. 9. Histograms of the uncertainties of the parameters derived from (a) the method in the classic literature and (b) the method based on the PHOENIX model.

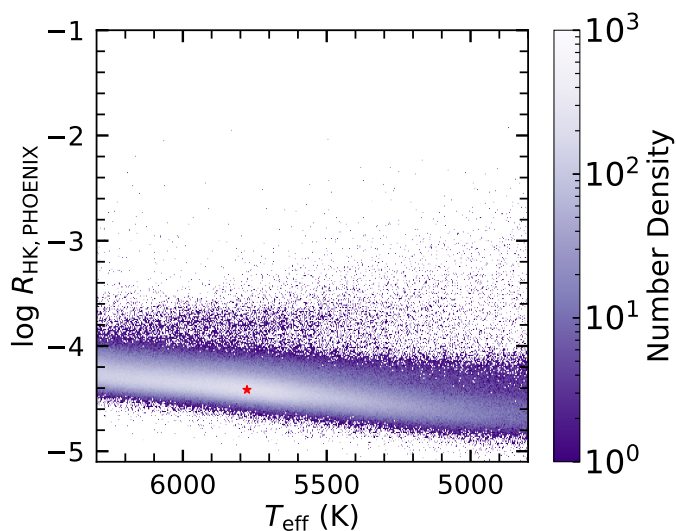


Fig. 10. Scatter diagram of $\log R_{\text{HK,PHOENIX}}$ with T_{eff} for all of solar-like stars investigated in this work. The color scale represents the density of data points. The $R_{\text{HK,PHOENIX}}$ value of the Sun is marked with a (\star) symbol.

$$\log R'_{\text{HK,PHOENIX}} = 1.595 - 3.166 \log g + 0.384(\log g)^2, \quad (28)$$

$$\log R'_{\text{HK,PHOENIX}} = -4.912 - 0.065[\text{Fe}/\text{H}] + 7.894 \times 10^{-3}[\text{Fe}/\text{H}]^2. \quad (29)$$

As shown in Figure 12, the median values of $\log R'_{\text{HK,PHOENIX}}$ with T_{eff} have a minimum at about $T_{\text{eff}} = 5500$ K, while the dependence of the median values of $\log R'_{\text{HK,PHOENIX}}$ on $\log g$ and $[\text{Fe}/\text{H}]$ is relatively weak. Besides, it can be seen that the solar $\log R'_{\text{HK,PHOENIX}}$ value is approximately on the fitting lines of the median $\log R'_{\text{HK,PHOENIX}}$ values for all the three parameters, and the value of solar chromospheric activity index is located at the midpoint of the solar-like star sample. This result based on our

extensive archive support the view that the dynamo mechanism of solar-like stars is generally consistent with the Sun.

Henry et al. (1996) classified the stellar chromospheric activity into four levels: very active ($\log R'_{\text{HK}}$ larger than -4.20), active ($\log R'_{\text{HK}}$ from -4.75 to -4.20), inactive ($\log R'_{\text{HK}}$ from -5.10 to -4.75) and very inactive ($\log R'_{\text{HK}}$ less than -5.10). Following this classification, based on the $\log R'_{\text{HK,PHOENIX}}$ values of 861,505 stars, we can obtain the proportions of very active, active, inactive and very inactive solar-like stars as 1.03%, 21.68%, 65.27% and 12.03%, respectively. While for the values of $\log R'_{\text{HK,classic}}$, the proportions are 1.07%, 24.53%, 62.98% and 11.41%, respectively. The proportions of stars in the different stellar chromospheric activity classes are 2.6%, 27.1%, 62.5% and 7.9% in Henry et al. (1996), and 1.2%, 28.5%, 66.9% and 3.5% in Gomes da Silva et al. (2021). When using a threshold of $\log R'_{\text{HK}} = -4.75$ to classify stars as active and inactive, Henry et al. (1996) and Gomes da Silva et al. (2021) found that 29.7% stars are classified as active. Classifying the solar-like stars with $\log R'_{\text{HK,PHOENIX}} = -4.75$ and $\log R'_{\text{HK,classic}} = -4.75$, we can obtain the proportions of active solar-like stars as 22.71% and 25.60%, respectively. The proportions are relatively consistent with the results of Henry et al. (1996) and Gomes da Silva et al. (2021).

In Figure 13, we show the distributions of $\log R'_{\text{HK,PHOENIX}}$ values in the T_{eff} vs. $\log g$, T_{eff} vs. $[\text{Fe}/\text{H}]$, and $[\text{Fe}/\text{H}]$ vs. $\log g$ parameters spaces. The stellar chromospheric activity levels of very active, active, inactive, and very inactive are indicated by different colors. It can be seen from Figure 13 that the higher the stellar chromospheric activity levels, the narrower the distribution areas in the parameters spaces. Since the LAMOST LRS spectra of solar-like stars with determined stellar atmospheric parameters are sufficient, we further investigate the relations between the proportions of solar-like stars with different chromospheric activity levels (classified by $R'_{\text{HK,PHOENIX}}$) and the stellar atmospheric parameters (T_{eff} , $\log g$ and $[\text{Fe}/\text{H}]$). The proportions of very active, active, inactive and very inactive solar-like stars with different stellar atmospheric parameters are shown in Figure 14. The proportions values in Figure 14 are obtained by dividing the T_{eff} , $\log g$ and $[\text{Fe}/\text{H}]$ into bins with step size of 100 K, 0.1 dex and 0.1 dex, respectively; and the central values of each

Table 3. Columns in the catalog of the database.

Column	Unit	Description
obsid		Unique observation identifier of LAMOST LRS spectrum
obsdate		Spectral observation date
fitsname		FITS file name of LAMOST LRS spectrum
snrg		Signal-to-noise ratio in the g band (S/N_g) of LAMOST LRS spectrum
snrr		Signal-to-noise ratio in the r band (S/N_r) of LAMOST LRS spectrum
teff	K	Effective temperature (T_{eff}) derived from the LASP
teff_err	K	Uncertainty of T_{eff} derived from the LASP
logg	dex	Surface gravity ($\log g$) derived from the LASP
logg_err	dex	Uncertainty of $\log g$ derived from the LASP
feh	dex	Metallicity ($[\text{Fe}/\text{H}]$) derived from the LASP
feh_err	dex	Uncertainty of $[\text{Fe}/\text{H}]$ derived from the LASP
rv	km/s	Radial velocity (V_r) derived from the LASP
rv_err	km/s	Uncertainty of V_r derived from the LASP
ra_obs	degree	Right ascension (RA) of fiber pointing
dec_obs	degree	Declination (DEC) of fiber pointing
gaia_source_id		Source identifier in Gaia DR3 catalog
gaia_g_mean_mag		G magnitude in Gaia DR3 catalog
S_tri*		S_{tri} index of LAMOST LRS
S_tri_err*		Uncertainty of S_{tri}
S_MWO*		S_{MWO}
S_MWO_err*		Uncertainty of S_{MWO}
log_R_HK_classic*		$\log R_{\text{HK,classic}}$
log_R_HK_classic_err*		Uncertainty of $\log R_{\text{HK,classic}}$
log_R_p_HK_classic*		$\log R'_{\text{HK,classic}}$
log_R_p_HK_classic_err*		Uncertainty of $\log R'_{\text{HK,classic}}$
log_R_HK_PHOENIX*		$\log R_{\text{HK,PHOENIX}}$
log_R_HK_PHOENIX_err*		Uncertainty of $\log R_{\text{HK,PHOENIX}}$
log_R_p_HK_PHOENIX*		$\log R'_{\text{HK,PHOENIX}}$
log_R_p_HK_PHOENIX_err*		Uncertainty of $\log R'_{\text{HK,PHOENIX}}$

Notes. The columns denoted by an asterisk represent the parameters estimated in this work, and the remaining columns utilized in our research are collected from the data release of LAMOST DR8 V2.0. The detailed definitions of the chromospheric activity parameters can be seen in Section 3.

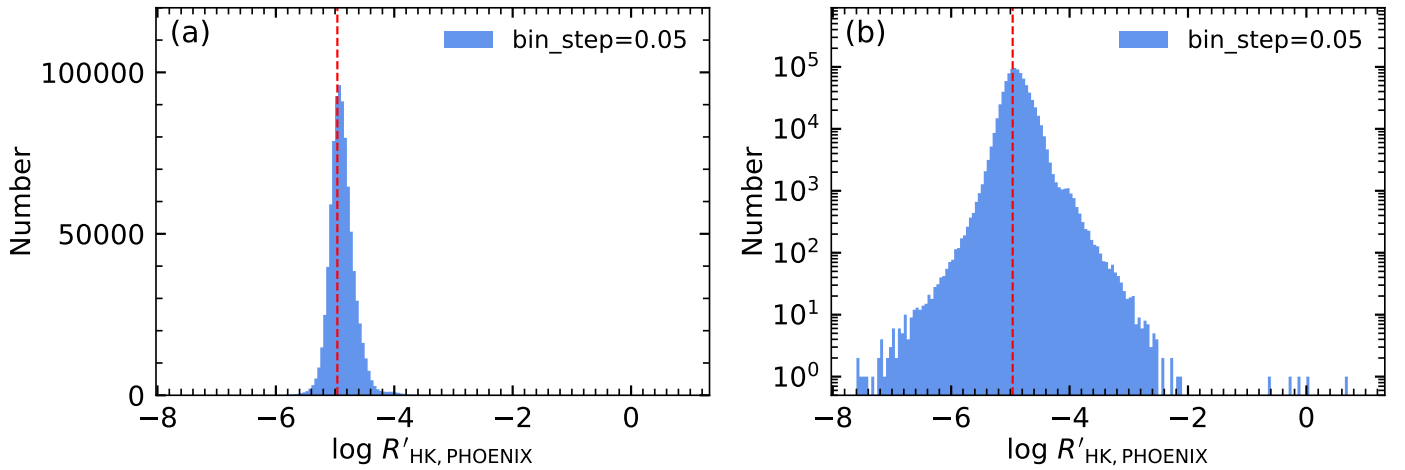


Fig. 11. Histograms of the $\log R'_{\text{HK,PHOENIX}}$ values for the solar-like stars investigated in this work through (a) linear-scale and (b) logarithmic-scale vertical axes. The $\log R'_{\text{HK,PHOENIX}}$ value of the Sun (-4.9599 as given in Section 3.3) is indicated by a vertical dashed line.

bin are used to represent the corresponding stellar atmospheric parameters.

Figure 14(a) shows that the proportions of inactive solar-like stars exhibit a relatively stable trend within the T_{eff} range of 4800 to 6000 K. For the very inactive solar-like stars, there is an increasing trend in the proportions as the T_{eff} decreases within the

T_{eff} range from 6300 to 5650 K, and the proportions decrease within the T_{eff} range from 5650 to 4800 K. In contrast, the proportions of active solar-like stars exhibit a decreasing trend with decreasing T_{eff} from 6300 to 5650 K, and the decreasing trend of the proportions of active solar-like stars is reversed for T_{eff} lower than 5650 K. The proportions of very active solar-like stars

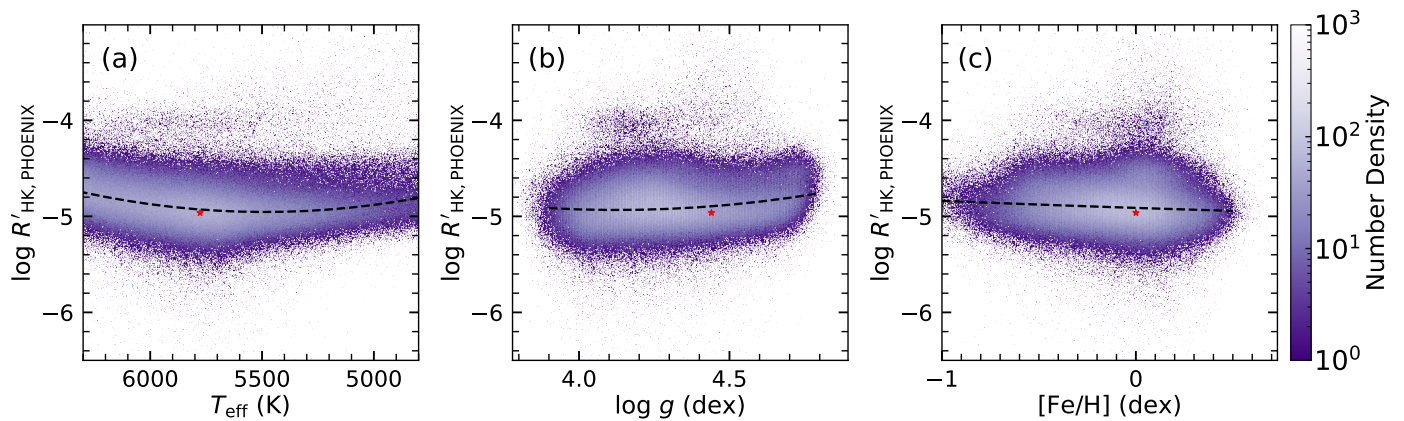


Fig. 12. Scatter diagrams of $\log R'_{\text{HK,PHOENIX}}$ with (a) T_{eff} , (b) $\log g$, and (c) $[\text{Fe}/\text{H}]$ for the solar-like stars investigated in this work. The position of the solar $\log R'_{\text{HK,PHOENIX}}$ in these diagrams is denoted by a (\star) symbol. The black dashed lines represent the fitted median values of $\log R'_{\text{HK,PHOENIX}}$. The color scale indicates the number density. Some values of $\log R'_{\text{HK,PHOENIX}}$ outside the displayed range are considered insignificant for the overall distribution and are therefore not shown.

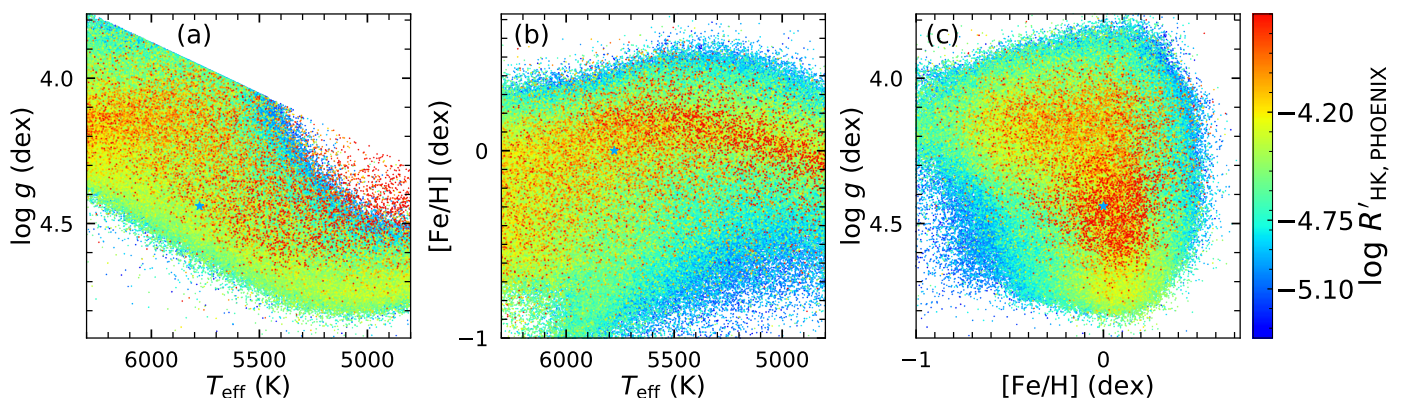


Fig. 13. Distributions of $\log R'_{\text{HK,PHOENIX}}$ values in (a) T_{eff} vs. $\log g$, (b) T_{eff} vs. $[\text{Fe}/\text{H}]$, and (c) $[\text{Fe}/\text{H}]$ vs. $\log g$ parameter spaces for the solar-like stars investigated in this work. The stellar chromospheric activity levels of very active, active, inactive and very inactive are indicated by different colors. The values of $\log R'_{\text{HK,PHOENIX}}$ that fall outside the range of the color bar are represented by the boundary value. The data points with smaller $\log R'_{\text{HK,PHOENIX}}$ are overlaid by the data points with larger $\log R'_{\text{HK,PHOENIX}}$. The positions of the solar $\log R'_{\text{HK,PHOENIX}}$ are marked in the diagrams with a (\star) symbol colored in accordance with the solar activity level.

are almost stable for $T_{\text{eff}} > 5900$ K, while they increase for $T_{\text{eff}} < 5600$ K. The minimum value of the proportions of very active solar-like stars is around $T_{\text{eff}} = 5700$ K. Based on the proportions of active and very active solar-like stars, we conclude that the occurrence rate of high levels of chromospheric activity is lower among the stars with effective temperatures between 5600 and 5900 K.

The relations between $\log g$ and the proportions of solar-like stars with different chromospheric activity levels are displayed in Figure 14(b). The proportions of different chromospheric activity levels of solar-like stars appear to be relatively stable in the range of $3.9 < \log g < 4.5$ dex. When $\log g > 4.5$ dex, the proportions of active solar-like stars exhibits an increasing trend, whereas the spectral ratios of very inactive, inactive and very active solar-like stars decrease.

Gray et al. (2006) and Hinkel et al. (2017) detected that the distribution of $\log R'_{\text{HK}}$ varies among stars with different levels of metallicity, and the bimodal distribution (Vaughan & Preston 1980) is observed in dwarf stars with $[\text{Fe}/\text{H}]$ greater than -0.2 dex. In the research of Jenkins et al. (2008), the majority of stars with $[\text{Fe}/\text{H}] > 0.1$ dex were found to be inactive. In Figure 11, the bimodal distribution of $\log R'_{\text{HK}}$ does not exist in our solar-like star sample of LAMOST LRS. However, as shown in Figure 14(c), when $[\text{Fe}/\text{H}] > 0.1$ dex, there is a decrease in

the proportions of active solar-like stars. This decreasing trend ceases and the proportions of active solar-like stars becomes relatively stable when $[\text{Fe}/\text{H}] = 0.3$ dex.

5. Summary and Conclusion

In this work, we identify 1,122,495 high-quality LRS spectra of solar-like stars from LAMOST DR8 and provide a database of stellar chromospheric activity parameters based on this spectral sample. The database contains the stellar chromospheric activity parameters S_{tri} , S_{MWO} , R_{HK} and R'_{HK} , as well as their uncertainties. R_{HK} and R'_{HK} are derived from the method in the classic literature (denoted with classic) and the method based on the PHOENIX model (denoted with PHOENIX). When converting the S_{MWO} to the bolometric calibrated index R_{HK} , the $R_{\text{HK,classic}}$ values are estimated based on the bolometric factor C_{cf} from Rutten (1984) and the K factor from Middelkoop (1982), while the $R_{\text{HK,PHOENIX}}$ values are derived from the stellar surface flux \mathcal{F}_{RV} . The values of $R_{\text{HK,PHOENIX}}$ are approximately $\beta = 1.6$ times larger than the values of $R_{\text{HK,classic}}$. For the corresponding photospheric contribution R_{phot} , the $R_{\text{phot,classic}}$ are deduced based on Noyes et al. (1984), and the $R_{\text{phot,PHOENIX}}$ are scaled by β times from the $R_{\text{phot,classic}}$. The bolometric and photospheric calibrated chromospheric activity index R'_{HK} is consequently de-

rived by eliminating the photospheric contribution from R_{HK} . Our calculations show that $\log R_{\text{HK,PHOENIX}}$ and $\log R'_{\text{HK,PHOENIX}}$ are approximately linearly correlated with $\log R_{\text{HK,classic}}$ and $\log R'_{\text{HK,classic}}$, respectively.

We explore the overall properties of stellar chromospheric activity based on the 861,505 solar-like stars in the database. The results show that the median values of $\log R'_{\text{HK,PHOENIX}}$ with T_{eff} have a minimum at about $T_{\text{eff}} = 5500$ K, while the dependence of the median values of $\log R'_{\text{HK,PHOENIX}}$ on $\log g$ and $[\text{Fe}/\text{H}]$ is relatively weak. The value of solar chromospheric activity index is located at the midpoint of the solar-like star sample. This result from our extensive archive support the view that the dynamo mechanism of solar-like stars is generally consistent with the Sun. The absence of VP gap in the distribution of chromospheric activity for our solar-like stars could be attributed to three possible factors: 1) a gradual diminishing of chromospheric activity during the evolution of solar-like stars; 2) the influence of different stellar properties on the bimodal distribution of the chromospheric activity within our samples, which should be explored in more detail in the future, or 3) the loss of some information in the spectral profile due to the limited resolution of LAMOST LRS spectra.

We explore the proportions of solar-like stars with different chromospheric activity levels (very active, active, inactive and very inactive). Based on the values of $\log R'_{\text{HK,PHOENIX}}$, we can obtain the proportions of very active, active, inactive and very inactive solar-like stars as 1.03%, 21.68%, 65.27% and 12.03%, respectively. While for the values of $\log R'_{\text{HK,classic}}$, the proportions are 1.07%, 24.53%, 62.98% and 11.41%, respectively. It is observed that the higher the stellar chromospheric activity levels, the narrower the distribution areas in the T_{eff} vs. $\log g$, T_{eff} vs. $[\text{Fe}/\text{H}]$, and $[\text{Fe}/\text{H}]$ vs. $\log g$ parameters spaces.

We further investigate the relation between the proportions of solar-like stars with different chromospheric activity levels (classified by $R'_{\text{HK,PHOENIX}}$) and the stellar atmospheric parameters (T_{eff} , $\log g$ and $[\text{Fe}/\text{H}]$). Based on the proportions of active and very active solar-like stars, it is concluded that the occurrence rate of high levels of chromospheric activity is lower among the stars with effective temperatures between 5600 and 5900 K. It is found that when $\log g > 4.5$ dex, the proportions of active solar-like stars exhibits an increasing trend, whereas the proportions of very inactive, inactive and very active solar-like stars decrease. It is discovered that there is a decrease in the proportions of active solar-like stars when $[\text{Fe}/\text{H}] > 0.1$ dex. This decreasing trend ceases and the proportions of active solar-like stars becomes relatively stable when $[\text{Fe}/\text{H}] = 0.3$ dex.

The chromospheric activity database of the LAMOST LRS spectra of solar-like stars provided in this work includes the most commonly used chromospheric activity parameters such as S_{MWO} , R_{HK} and R'_{HK} . The relationship between chromospheric activity and other stellar magnetic manifestation (such as stellar rotation period and age) can be further investigated. Additionally, the database can be used to investigate the relationship between stellar and solar activity for a better understanding of the stellar-solar connection. The database may also contribute to the discovery of new solar-type stars accommodating potentially habitable exoplanetary systems.

Acknowledgements. This work is supported by the National Key R&D Program of China (2019YFA0405000) and the National Natural Science Foundation of China (12073001 and 11973059). W.Z. and J.Z. thank the support of the Anhui Project (Z010118169). H.H. acknowledges the CAS Strategic Pioneer Program on Space Science (XDA15052200) and the B-type Strategic Priority Program of the Chinese Academy of Sciences (XDB41000000). Guoshoujing Telescope (the Large Sky Area Multi-Object Fiber Spectroscopic Telescope, LAMOST) is

a National Major Scientific Project built by the Chinese Academy of Sciences. Funding for the project has been provided by the National Development and Reform Commission. LAMOST is operated and managed by the National Astronomical Observatories, Chinese Academy of Sciences.

References

- Ahumada, R., Allende Prieto, C., Almeida, A., et al. 2020, *ApJS*, 249, 3
Allard, F. 2014, in *Exploring the Formation and Evolution of Planetary Systems*, ed. M. Booth, B. C. Matthews, & J. R. Graham, Vol. 299, 271–272
Allard, F. & Hauschildt, P. H. 1995, *ApJ*, 445, 433
Amard, L., Roquette, J., & Matt, S. P. 2020, *MNRAS*, 499, 3481
Astudillo-Defru, N., Delfosse, X., Bonfils, X., et al. 2017, *A&A*, 600, A13
Bai, Z.-R., Zhang, H.-T., Yuan, H.-L., et al. 2021, *Research in Astronomy and Astrophysics*, 21, 249
Baliunas, S. L., Donahue, R. A., Soon, W. H., et al. 1995, *ApJ*, 438, 269
Booth, R. S., Poppenhaeger, K., Watson, C. A., et al. 2020, *MNRAS*, 491, 455
Boro Saikia, S., Marvin, C. J., Jeffers, S. V., et al. 2018, *A&A*, 616, A108
Boudreaux, T. M., Newton, E. R., Mondrik, N., Charbonneau, D., & Irwin, J. 2022, *ApJ*, 929, 80
Brown, E. L., Jeffers, S. V., Marsden, S. C., et al. 2022, *MNRAS*, 514, 4300
Casagrande, L., Ramírez, I., Meléndez, J., Bessell, M., & Asplund, M. 2010, *A&A*, 512, A54
Cayrel de Strobel, G. 1996, *A&A Rev.*, 7, 243
Ciddor, P. E. 1996, *Appl. Opt.*, 35, 1566
Cincunegui, C., Díaz, R. F., & Mauas, P. J. D. 2007, *A&A*, 469, 309
Cui, X.-Q., Zhao, Y.-H., Chu, Y.-Q., et al. 2012, *Research in Astronomy and Astrophysics*, 12, 1197
de Grijs, R. & Kamath, D. 2021, *Universe*, 7, 440
Duncan, D. K., Vaughan, A. H., Wilson, O. C., et al. 1991, *ApJS*, 76, 383
Egeland, R., Soon, W., Baliunas, S., et al. 2017, *ApJ*, 835, 25
Gaia Collaboration, Vallenari, A., Brown, A. G. A., et al. 2023, *A&A*, 674, A1
Gomes da Silva, J., Santos, N. C., Adibekyan, V., et al. 2021, *A&A*, 646, A77
Gray, R. O., Corbally, C. J., Garrison, R. F., et al. 2006, *AJ*, 132, 161
Gray, R. O., Corbally, C. J., Garrison, R. F., McFadden, M. T., & Robinson, P. E. 2003, *AJ*, 126, 2048
Gustafsson, B., Edvardsson, B., Eriksson, K., et al. 2008, *A&A*, 486, 951
Hall, J. C. 2008, *Living Reviews in Solar Physics*, 5, 2
Hall, J. C., Lockwood, G. W., & Skiff, B. A. 2007, *AJ*, 133, 862
Han, H., Wang, S., Bai, Y., et al. 2023, *ApJS*, 264, 12
Hardorp, J. 1980, *A&A*, 91, 221
Hartmann, L., Soderblom, D. R., Noyes, R. W., Burnham, N., & Vaughan, A. H. 1984, *ApJ*, 276, 254
He, H., Zhang, H., Wang, S., Yang, S., & Zhang, J. 2021, *Research Notes of the AAS*, 5, 6
He, H., Zhang, W., Zhang, H., et al. 2023, *Ap&SS*, 368, 63
Henry, T. J., Soderblom, D. R., Donahue, R. A., & Baliunas, S. L. 1996, *AJ*, 111, 439
Hinkel, N. R., Mamajek, E. E., Turnbull, M. C., et al. 2017, *ApJ*, 848, 34
Huang, X., He, Y., Bai, Z., et al. 2024, *ApJS*, 272, 6
Husser, T. O., Wende-von Berg, S., Dreizler, S., et al. 2013, *A&A*, 553, A6
Isaacson, H. & Fischer, D. 2010, *ApJ*, 725, 875
Jenkins, J. S., Jones, H. R. A., Pavlenko, Y., et al. 2008, *A&A*, 485, 571
Jenkins, J. S., Jones, H. R. A., Tinney, C. G., et al. 2006, *MNRAS*, 372, 163
Jenkins, J. S., Murgas, F., Rojo, P., et al. 2011, *A&A*, 531, A8
Johnson, H. L. 1966, *ARA&A*, 4, 193
Karoff, C., Metcalfe, T. S., Montet, B. T., et al. 2019, *MNRAS*, 485, 5096
Lançon, A., Gonneau, A., Verro, K., et al. 2021, *A&A*, 649, A97
Linsky, J. L., Worden, S. P., McClintock, W., & Robertson, R. M. 1979, *ApJS*, 41, 47
Lorenzo-Oliveira, D., Freitas, F. C., Meléndez, J., et al. 2018, *A&A*, 619, A73
Lovis, C., Dumusque, X., Santos, N. C., et al. 2011, *arXiv e-prints*, arXiv:1107.5325
Luo, A. L., Zhang, H.-T., Zhao, Y.-H., et al. 2012, *Research in Astronomy and Astrophysics*, 12, 1243
Luo, A. L., Zhao, Y.-H., Zhao, G., et al. 2015, *Research in Astronomy and Astrophysics*, 15, 1095
Mamajek, E. E. & Hillenbrand, L. A. 2008, *ApJ*, 687, 1264
Marvin, C. J., Reiners, A., Anglada-Escudé, G., Jeffers, S. V., & Boro Saikia, S. 2023, *A&A*, 671, A162
Melbourne, K., Youngblood, A., France, K., et al. 2020, *AJ*, 160, 269
Middelkoop, F. 1982, *A&A*, 107, 31
Mittag, M., Schmitt, J. H. M. M., & Schröder, K. P. 2013, *A&A*, 549, A117
Munari, U., Sordo, R., Castelli, F., & Zwitter, T. 2005, *A&A*, 442, 1127
Noyes, R. W., Hartmann, L. W., Baliunas, S. L., Duncan, D. K., & Vaughan, A. H. 1984, *ApJ*, 279, 763
Oranje, B. J. 1983, *A&A*, 124, 43
Pace, G. 2013, *A&A*, 551, L8

Pérez Martínez, M. I., Schröder, K. P., & Hauschildt, P. 2014, MNRAS, 445, 270
Ramírez, I., Michel, R., Sefako, R., et al. 2012, ApJ, 752, 5
Rutten, R. G. M. 1984, A&A, 130, 353
Rutten, R. G. M. 1987, A&A, 177, 131
Sowmya, K., Shapiro, A. I., Witzke, V., et al. 2021, ApJ, 914, 21
Suárez Mascareño, A., Rebolo, R., González Hernández, J. I., & Esposito, M. 2015, MNRAS, 452, 2745
Vaughan, A. H. & Preston, G. W. 1980, PASP, 92, 385
Vaughan, A. H., Preston, G. W., & Wilson, O. C. 1978, PASP, 90, 267
Virtanen, P., Gommers, R., Oliphant, T. E., et al. 2020, Nature Methods, 17, 261
Wilson, O. C. 1968, ApJ, 153, 221
Wilson, O. C. 1978, ApJ, 226, 379
Wright, J. T., Marcy, G. W., Butler, R. P., & Vogt, S. S. 2004, ApJS, 152, 261
York, D. G., Adelman, J., Anderson, John E., J., et al. 2000, AJ, 120, 1579
Zhang, J., Bi, S., Li, Y., et al. 2020, ApJS, 247, 9
Zhang, J., Zhao, J., Oswald, T. D., et al. 2019, ApJ, 887, 84
Zhang, W., Zhang, J., He, H., et al. 2022, ApJS, 263, 12
Zhao, G., Zhao, Y.-H., Chu, Y.-Q., Jing, Y.-P., & Deng, L.-C. 2012, Research in Astronomy and Astrophysics, 12, 723

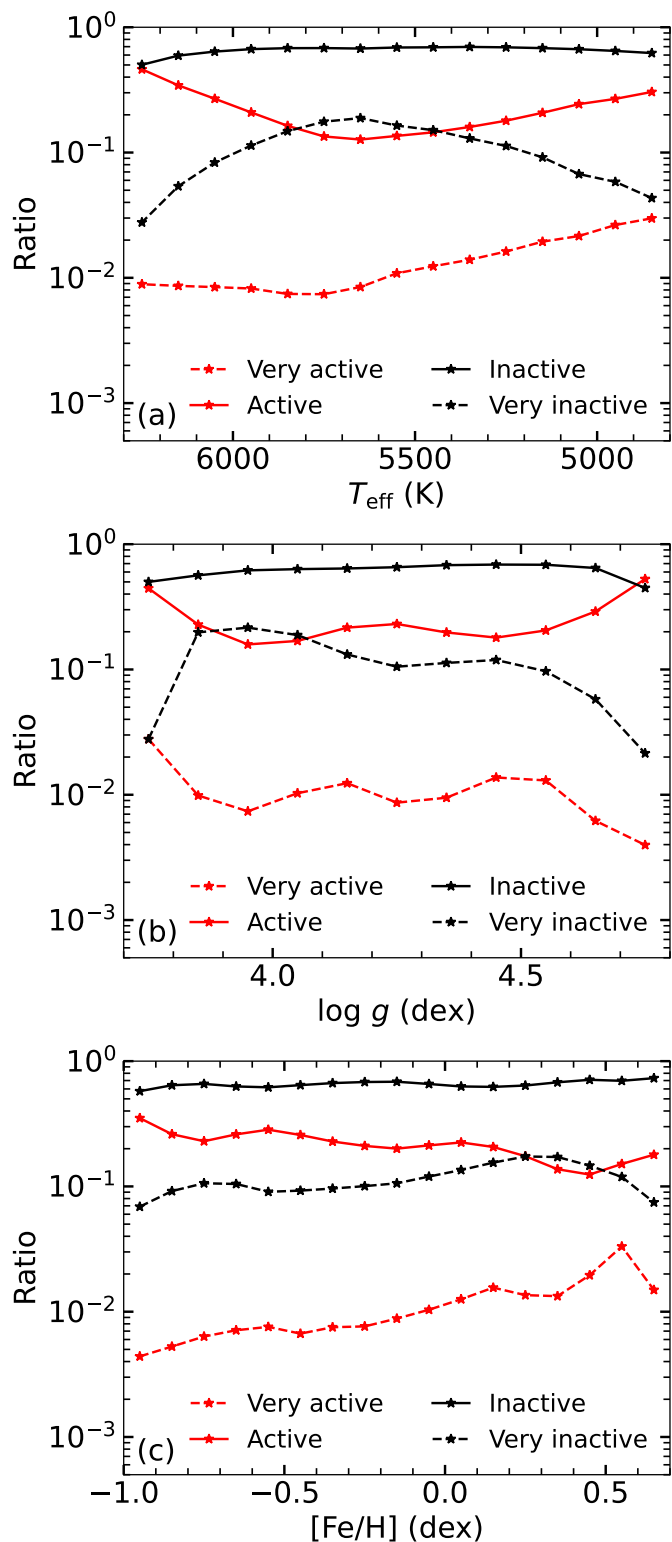


Fig. 14. Relations of the proportions of very active (red dashed line), active (red line), inactive (black line) and very inactive (black dashed line) solar-like stars with (a) T_{eff} , (b) $\log g$ and (c) $[\text{Fe}/\text{H}]$. The proportions values are obtained by dividing the T_{eff} , $\log g$ and $[\text{Fe}/\text{H}]$ into bins with step size of 100 K, 0.1 dex and 0.1 dex, respectively, and the central values of each bin are used to represent the corresponding stellar atmospheric parameters.

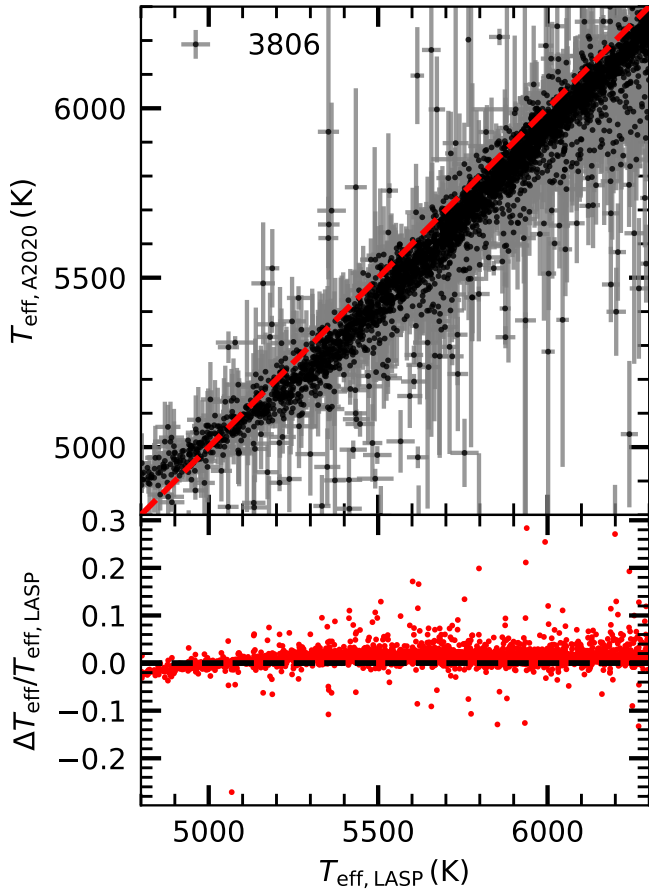


Fig. A.1. The distribution of the $T_{\text{eff,LASP}}$ values and the $T_{\text{eff,A2020}}$ values for 3806 common stars, where $T_{\text{eff,A2020}}$ denotes the effective temperature in Amard et al. (2020). The red dashed line represents the case where $T_{\text{eff,LASP}}$ equals $T_{\text{eff,A2020}}$. Error bars are indicated for data points that have specified uncertainty values. The lower panel displays the distribution of $\Delta T_{\text{eff}}/T_{\text{eff,LASP}}$ against $T_{\text{eff,LASP}}$, where $\Delta T_{\text{eff}} = T_{\text{eff,LASP}} - T_{\text{eff,A2020}}$.

Appendix A: Accuracy of Stellar Parameters

We identify 3806 common stars in Amard et al. (2020) and compare their effective temperature values with those in our database, as shown in Figure A.1. For T_{eff} in the range of 4800 to 6300 K, the T_{eff} values provided by LASP are approximately consistent with the results in Amard et al. (2020), generally with ΔT_{eff} less than 120 K. The $T_{\text{eff,A2020}}$ values are obtained from various observation instruments and are taken from the survey with the highest spectral resolution when the same sources were observed in multiple surveys (Amard et al. 2020). Differences in observation instruments and estimation methods would contribute to the discrepancies between $T_{\text{eff,LASP}}$ and $T_{\text{eff,A2020}}$. Although there are some differences between $T_{\text{eff,LASP}}$ and $T_{\text{eff,A2020}}$, the corresponding $\log R'_{\text{HK,PHOENIX}}$ values estimated based on $T_{\text{eff,LASP}}$ and $T_{\text{eff,A2020}}$ exhibit approximate consistency as shown in Figure A.2, where the $\Delta \log R'_{\text{HK,PHOENIX}}$ values are generally less than 0.05.

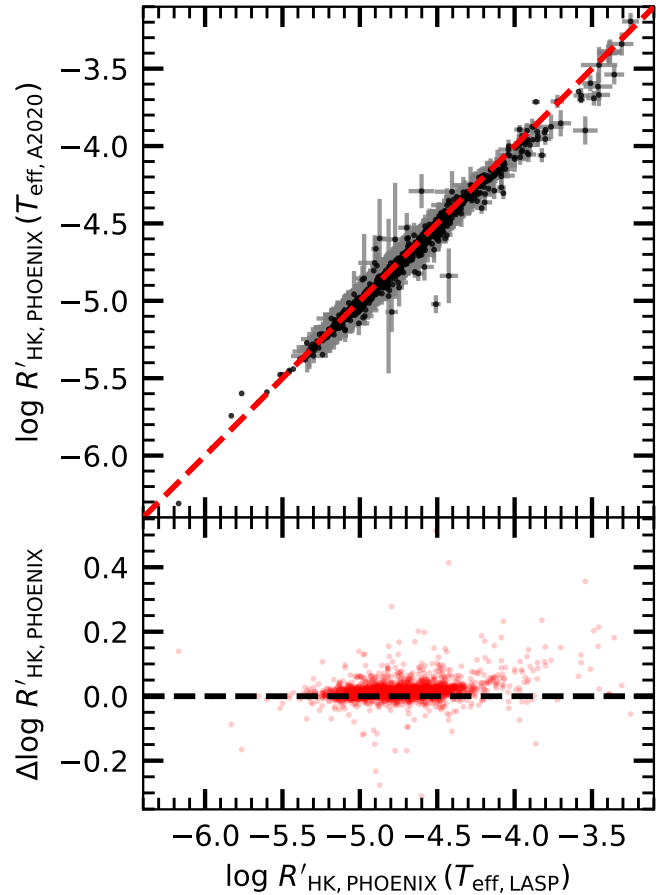


Fig. A.2. Scatter plot of $\log R'_{\text{HK,PHOENIX}}(T_{\text{eff,LASP}})$ versus $\log R'_{\text{HK,PHOENIX}}(T_{\text{eff,A2020}})$ for stars in Figure A.1. Error bars are displayed for data points with known uncertainty values. The red dashed line represents the ratio of $\frac{\log R'_{\text{HK,PHOENIX}}(T_{\text{eff,LASP}})}{\log R'_{\text{HK,PHOENIX}}(T_{\text{eff,A2020}})} = 1$. The lower panel shows the distribution of $\Delta \log R'_{\text{HK,PHOENIX}}$ against $\log R'_{\text{HK,PHOENIX}}(T_{\text{eff,LASP}})$.

Appendix B: Calibration of Chromospheric Activity Index

We cross-match the Gaia DR3 source identifier in this paper with stars in Wright et al. (2004), Isaacson & Fischer (2010), Boro Saikia et al. (2018) and Gomes da Silva et al. (2021), and find out 23 common stars (16 stars in Wright et al. 2004 and Isaacson & Fischer 2010 are also studied in Boro Saikia et al. 2018). Figure B.1 shows the distribution between $\log R'_{\text{HK,PHOENIX}}$ and $\log R'_{\text{HK,paper}}$. As can be seen in Figure B.1, our results show an approximate agreement with values from other instruments. The values used in Figure B.1 are recorded in Table B.1.

Appendix C: Distribution of Chromospheric Activity Index with multi-observation

The histogram of $\sigma_{\log R'_{\text{HK,PHOENIX}}}/\log R'_{\text{HK,PHOENIX}}$ for stars with more than one observation is shown in Figure C.1, where the $\sigma_{\log R'_{\text{HK,PHOENIX}}}$ represents the standard deviation of $\log R'_{\text{HK,PHOENIX}}$. The stars with $\sigma_{\log R'_{\text{HK,PHOENIX}}}/\log R'_{\text{HK,PHOENIX}} < 0.2$ account for 95.5% of the stars with more than one observation. Additionally, Figure C.2 displays the distributions of $\log R'_{\text{HK,PHOENIX}}$ with

Table B.1. Common stars for comparing $R'_{\text{HK,PHOENIX}}$ with $R'_{\text{HK,paper}}$ in Figure B.1.

Gaia DR3 Source ID	$\log R'_{\text{HK,PHOENIX}}$	$\delta \log R'_{\text{HK,PHOENIX}}$	$\log R'_{\text{HK,paper}}$	$\delta \log R'_{\text{HK,paper}}$	Star Name	Source
107774198474602368	-4.508228	0.010826	-4.37		HIP 10679	(1)
107774202769886848	-4.494861	0.015467	-4.41		HIP 10680	(1)
2482274463233174016	-4.765261	0.017813	-4.89		HIP 6712	(1)
2559181861327324928	-4.899986	0.021481	-5.05		HIP 6653	(1)
2568947762259903616	-4.859325	0.050142	-4.94		HIP 9035	(1)
2700327032273611264	-4.421454	0.010720	-4.36		HIP 107107	(1)
66838452861270272	-4.442698	0.011885	-4.377		HD 282954	(2)
77161217776670208	-4.505995	0.023880	-4.730		HD 13357	(2)
589826694824322176	-4.986656	0.039343	-4.972		HIP 46627	(2)
2482274463233174016	-4.765261	0.017813	-4.863		HD 8765	(2)
2559181861327324928	-4.899986	0.021481	-4.998		HD 8648	(2)
2664960072535183104	-4.873992	0.027421	-4.869		HD 219770	(2)
2700327032273611264	-4.421454	0.010720	-4.286		HD 206387	(2)
2838213864935858816	-4.451270	0.017570	-4.299		HD 219498	(2)
2868784136478476032	-5.065425	0.033502	-4.999		HIP 117386	(2)
3255358990147896704	-4.916303	0.071081	-4.962		HD 26257	(2)
66838452861270272	-4.442698	0.011885	-4.351		HD282954	(3)
77161217776670208	-4.505995	0.023880	-4.718		HD13357	(3)
77161217776670208	-4.505995	0.023880	-4.667		HIP10175	(3)
107774198474602368	-4.508228	0.010826	-4.275		HD14082B	(3)
107774198474602368	-4.508228	0.010826	-4.336		HIP10679	(3)
164088748804295168	-3.502017	0.025238	-3.912		HD281691	(3)
589826694824322176	-4.986656	0.039343	-5.017		HIP46627	(3)
2482274463233174016	-4.765261	0.017813	-4.841		HD8765	(3)
2482274463233174016	-4.765261	0.017813	-4.857		HIP6712	(3)
2559181861327324928	-4.899986	0.021481	-4.959		HD8648	(3)
2559181861327324928	-4.899986	0.021481	-4.990		HIP6653	(3)
2568947762259903616	-4.859325	0.050142	-4.863		HIP9035	(3)
2664960072535183104	-4.873992	0.027421	-4.800		HD219770	(3)
2700327032273611264	-4.421454	0.010720	-4.311		HD206387	(3)
2700327032273611264	-4.421454	0.010720	-4.353		HIP107107	(3)
2838213864935858816	-4.451270	0.017570	-4.277		HD219498	(3)
2868784136478476032	-5.065425	0.033502	-4.959		HIP117386	(3)
3231423481005237760	-4.924676	0.040069	-4.878		BD+000873	(3)
3255358990147896704	-4.916303	0.071081	-4.865		HD26257	(3)
3314440285393131008	-4.324742	0.014539	-4.468		HD27990	(3)
1153682508388170112	-5.162074	-9999	-5.0264	0.0094	WASP-24	(4)
2651240950559225728	-4.892375	0.012469	-4.9144	0.0047	HD 218249	(4)
2739638764856168192	-4.963751	0.040451	-4.9979	0.0059	HD 223854	(4)

References. (1) [Wright et al. \(2004\)](#); (2) [Isaacson & Fischer \(2010\)](#); (3) [Boro Saikia et al. \(2018\)](#); (4) [Gomes da Silva et al. \(2021\)](#);

T_{eff} (a), $\log g$ (b) and $[\text{Fe}/\text{H}]$ (c) for solar-like stars with more than one observation and $\sigma_{\log R'_{\text{HK,PHOENIX}}} / \log R'_{\text{HK,PHOENIX}} < 0.2$. The envelopes in Figure C.2 are similar to those in Figure 12. The distributions of $\log R'_{\text{HK,PHOENIX}}$ values in (a) T_{eff} vs. $\log g$, (b) T_{eff} vs. $[\text{Fe}/\text{H}]$, and (c) $[\text{Fe}/\text{H}]$ vs. $\log g$ parameter spaces for solar-like stars with more than one observation and $\sigma_{\log R'_{\text{HK,PHOENIX}}} / \log R'_{\text{HK,PHOENIX}} < 0.2$ are shown in Figure 13.

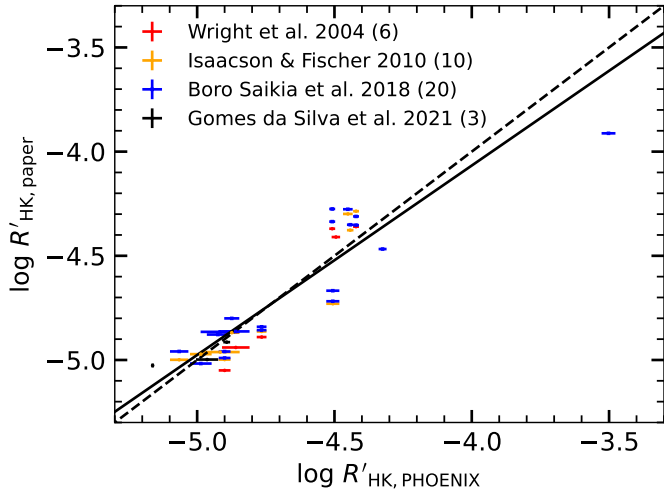


Fig. B.1. The distribution of $\log R'_{\text{HK,PHOENIX}}$ versus $\log R'_{\text{HK,paper}}$. The dashed line represents the case where the $\log R'_{\text{HK,PHOENIX}}$ is equal to $\log R'_{\text{HK,paper}}$, and the solid line is the linear fit between $\log R'_{\text{HK,PHOENIX}}$ and $\log R'_{\text{HK,paper}}$. Data points with quantified uncertainty are represented with error bars.

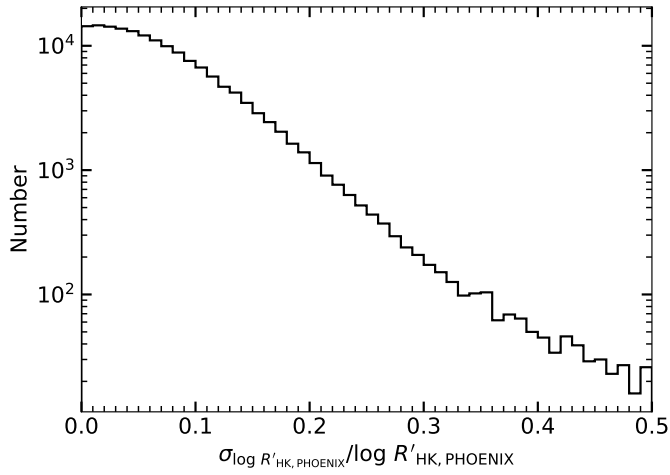


Fig. C.1. Histogram of $\sigma_{\log R'_{\text{HK,PHOENIX}}} / \log R'_{\text{HK,PHOENIX}}$ for solar-like stars with more than one observation, where the $\sigma_{\log R'_{\text{HK,PHOENIX}}}$ represents the standard deviation of $\log R'_{\text{HK,PHOENIX}}$.

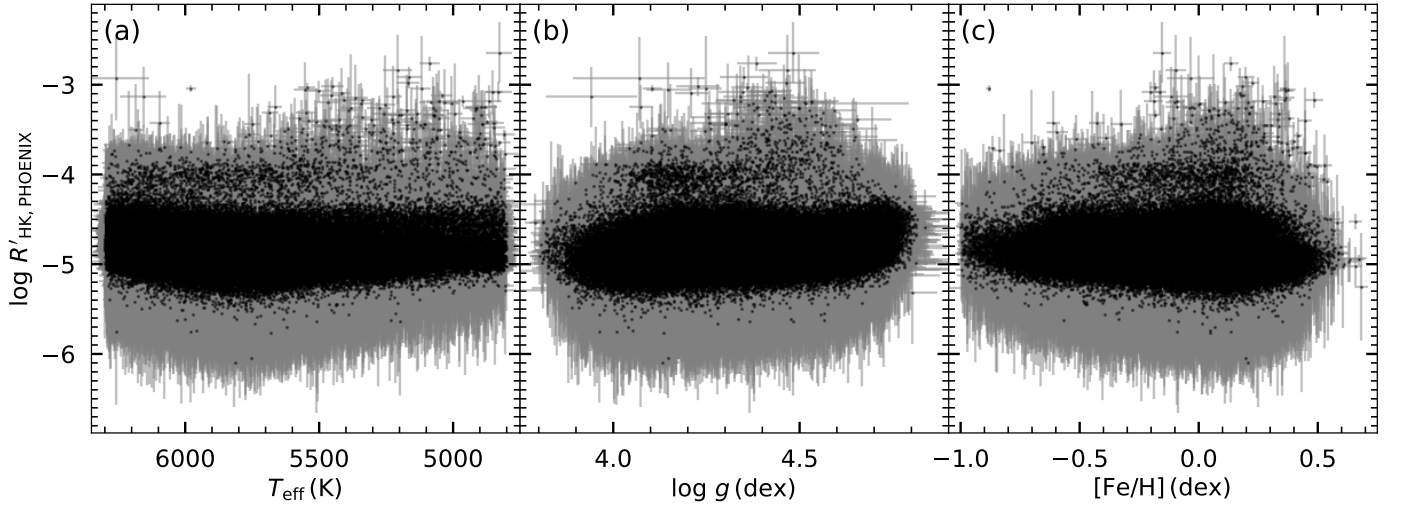


Fig. C.2. Distributions of $\log R'_{\text{HK,PHOENIX}}$ with (a) T_{eff} , (b) $\log g$ and (c) $[\text{Fe}/\text{H}]$ for solar-like stars with more than one observation and $\sigma_{\log R'_{\text{HK,PHOENIX}}} / \log R'_{\text{HK,PHOENIX}} < 0.2$. Error bars represent the standard deviation of $\log R'_{\text{HK,PHOENIX}}$.

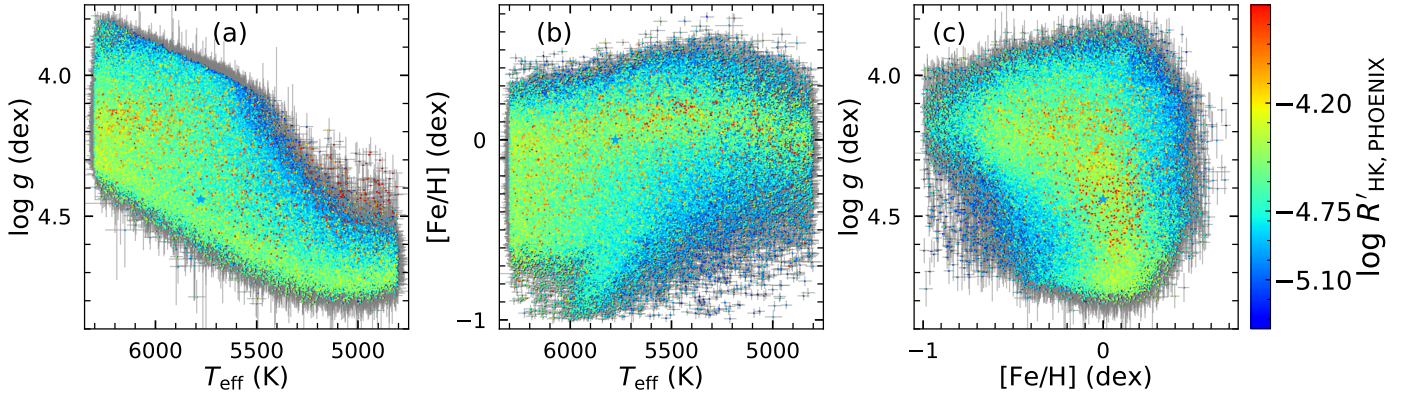


Fig. C.3. The distributions of $\log R'_{\text{HK,PHOENIX}}$ values in (a) T_{eff} vs. $\log g$, (b) T_{eff} vs. $[\text{Fe}/\text{H}]$, and (c) $[\text{Fe}/\text{H}]$ vs. $\log g$ parameter spaces for solar-like stars with more than one observation and $\sigma_{\log R'_{\text{HK,PHOENIX}}} / \log R'_{\text{HK,PHOENIX}} < 0.2$. The form of this image is similar to Figure 13, where the error bars belong to the bottom of the data point.